Journal of
Synchrotron Radiation

ISSN 0909-0495

Received 1 June 2006
Accepted 15 November 2006

XANES measurements of the rate of radiation damage to selenomethionine side chains

James M. Holton

Department of Biochemistry and Biophysics, University of California, San Francisco, CA 94158-2330, USA, and Advanced Light Source, Lawrence Berkeley National Laboratory, Berkeley, CA 94720, USA. E-mail: jmholton@lbl.gov

The radiation-induced disordering of selenomethionine (SeMet) side chains represents a significant impediment to protein structure solution. Not only does the increased *B*-factor of these sites result in a serious drop in phasing power, but some sites decay much faster than others in the same unit cell. These radiolabile SeMet side chains decay faster than high-order diffraction spots with dose, making it difficult to detect this kind of damage by inspection of the diffraction pattern. The selenium X-ray absorbance near-edge spectrum (XANES) from samples containing SeMet was found to change significantly after application of X-ray doses of 10–100 MGy. Most notably, the sharp 'white line' feature near the canonical Se edge disappears. The change was attributed to breakage of the Cγ—Se bond in SeMet. This spectral change was used as a probe to measure the decay rate of SeMet with X-ray dose in cryo-cooled samples. Two protein crystal types and 15 solutions containing free SeMet amino acid were examined. The damage rate was influenced by the chemical and physical condition of the sample, and the half-decaying dose for the selenium XANES signal ranged from 5 to 43 MGy. These decay rates were 34- to 3.8-fold higher than the rate at which the Se atoms interacted directly with X-ray photons, so the damage mechanism must be a secondary effect. Samples that cooled to a more crystalline state generally decayed faster than samples that cooled to an amorphous solid. The single exception was a protein crystal where a nanocrystalline cryoprotectant had a protective effect. Lowering the pH, especially with ascorbic or nitric acids, had a protective effect, and SeMet lifetime increased monotonically with decreasing sample temperature (down to 93 K). The SeMet lifetime in one protein crystal was the same as that of the free amino acid, and the longest SeMet lifetime measured was found in the other protein crystal type. This protection was found to arise from the folded structure of the protein molecule. A mechanism to explain observed decay rates involving the damaging species following the electric field lines around protein molecules is proposed.

Keywords: X-ray dose; protective solutes; pH and temperature effects; protein crystal structure; mechanism of radiation damage.

1. Introduction

1.1. Background

Protein crystallography data collection has often been associated with the specific disordering of methionine and other side chains (Weik *et al.*, 2000; Burmeister, 2000; Ravelli & McSweeney, 2000; Ravelli *et al.*, 2000; Banumathi *et al.*, 2004; Zwart *et al.*, 2004; Leiros *et al.*, 2006). The electron density of the -δ and Cε atoms of methionine and selenomethionine (SeMet) side chains was seen to disappear with dose. However, the electron density of the Cγ atom usually appeared stable and this change in electron density suggests that the Cγ—Se covalent bond is breaking. Moreover, SeMet side chains at different locations in the unit cell have been reported to have been damaged by different amounts after the same X-ray dose, implying significantly different decay rates. The mechanism behind the difference in decay rates is not clear (Garman & Nave, 2002; Nave & Garman, 2005), but the result is a heavy-atom contribution that changes phase as well as amplitude with dose. That is, as atoms are removed from the vector sum, the total phase of the heavy-atom contribution changes. This confounds most modern heavy-atom findings and phase determination techniques, which generally work with merged data and assume a static heavy-atom model. Efforts to solve a structure from data marred by this kind of damage usually end in failure. Indeed, only a fraction (10%) of

multi-wavelength anomalous diffraction (MAD) and single-wavelength anomalous diffraction (SAD) data collections lead to a solved structure, and radiation damage is a major cause of this (Holton, 2005). However, progress is being made. The program *SHARP* is capable of refining exponentially decaying sites (Bricogne *et al.*, 2005) against unmerged data, but a robust procedure for finding the initial positions of decaying heavy-atom sites has yet to be developed. The RIP phasing technique (Ravelli *et al.*, 2003, 2005; Nanao *et al.*, 2005) has been successful in using the specific changes in the structure to solve the phase problem, but care must be taken to measure the specific changes before global non-isomorphism sets in. Regardless of the phasing technique being utilized, the ability to predict or control the lifetime of SeMet and other sensitive species would increase the chances of success in determining protein structures.

1.2. Probes for radiation damage

Electron density is the most direct and relevant probe for specific damage in protein crystallography. However, quantitative decay rate information is difficult to extract from electron density data. The problem is that electron density data are prone to interference from systematic errors, such as model bias in the phases and the global loss of resolution with dose. For example, even if the Cγ—Se bond remains intact, the electron density peak height of the Se atom site will always diminish with dose because high-angle spots are vanishing. Such effects can be normalized by sharpening the map, but this introduces additional error. Moreover, electron density maps cannot be used to assay for damage before the structure has been solved, so an alternative probe would be useful for checking for damage during diffraction data collection.

X-ray absorption near-edge structure (XANES) can be used to monitor the breakdown of SeMet. XANES is not influenced by the loss of diffraction, and it is also not limited to conditions under which a particular crystal is stable. Studying the radiation damage behavior of free SeMet in solution is an important control for understanding the behavior of this side chain in the complex environment of protein crystals.

XANES is an established probe for the local bond environment of metal atoms (Durham *et al.*, 1981) and has been used to monitor radiation damage to metal sites in protein crystals (Yano *et al.*, 2005). The XANES procedure is commonly used at macromolecular crystallography beamlines in order to determine the best photon energies to use for MAD and SAD data collection. In this case the interest is in the energies of strongest absorption and dispersion, and the chemical information in the near-edge fine structure is not routinely used. XANES data are collected by scanning the incident photon energy across an X-ray absorption edge of the metal of interest and the absorption of the metal is (usually) measured by counting the fluorescent photons emitted by the metal. Incident photons with enough energy will excite an inner-shell electron of the metal to one of the outer shells or even into free space. The electron cloud in and around the metal will determine the accessible final energy states for the excited core electron. Transitions to more accessible energy states have higher probabilities so atoms interact more often with photons of energy equal to the difference in energy between the core and unoccupied outer orbitals. After this transition, the empty core orbital will be filled by an outer-shell electron. A fixed fraction of these core-filling transitions generate a fluorescent X-ray photon (McMaster *et al.*, 1969), so the amount of fluorescence is directly proportional to the absorbance. Therefore, the fluorescence-monitored absorbance spectrum contains information about the electron cloud surrounding the metal.

XANES of selenium compounds has been shown to be a powerful tool for identifying and quantifying a variety of selenium compounds as environmental contaminants in complex samples (Pickering *et al.*, 1995, 1999; Van Fleet-Stalder *et al.*, 2000; Sarret *et al.*, 2005). The so-called 'white line' peak feature at the absorption edge is particularly sensitive to the valence state of the Se atom; Pickering *et al.* (1995) describe the 'white line' as a $1s \rightarrow 4p$ transition. Binding partner atoms draw electrons out of these $4p$ orbitals (increasing the probability of a $1s \rightarrow 4p$ transition) leading to enhanced absorption and a peak in the XANES spectrum. A decrease in the intensity of the white line is consistent with a decreased number of bonds to the Se atom. A bond breakage such as the kind commonly observed in electron density of a radiation-damaged SeMet side chain would certainly remove the electron-withdrawing influence of the Cγ on the Se atom, and the white line of SeMet is indeed abolished by a large X-ray dose (see Fig. 1).

An important caveat of probing SeMet integrity with XANES is that no bidirectional connection has been made between XANES and electron density maps. A change in the

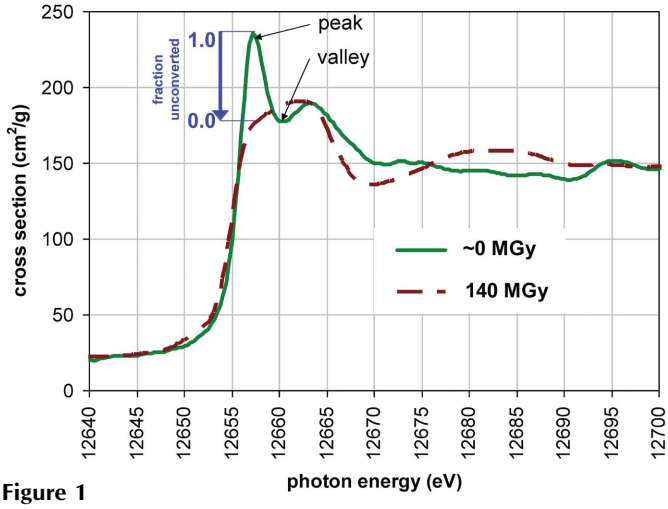

Figure 1
XANES spectra from a 25 m*M* aqueous solution of SeMet in 25% glycerol at 93 K. These spectra indicate the measured photoabsorption cross section of Se to photons of the indicated energy. The solid green spectrum was taken before the sample absorbed any significant dose (<1 MGy). The dashed brown line is a repeat of the same spectrum after the sample had absorbed a large dose (140 MGy). It is clear from these spectra that absorbed dose has an impact on XANES. The most prevalent change appears to be the loss of the so-called 'white line' peak absorbance. The height of the 'white line' peak (arrow) was used as the probe for the loss of the Se—C covalent bond.

height of the white line from SeMet is a necessary consequence of breaking the Cγ—Se bond but it is not sufficient evidence that the Cγ—Se bond has broken. For example, the end product of breaking the Se—Cε bond is expected to have an identical XANES spectrum. Other chemical changes are certainly possible, but the overall shape of the XANES spectrum will betray the presence of a new damage product species that has a different Se bonding environment than the Cγ—Se bond breakage product. These telltale changes can be seen in XANES spectra from reference compounds (Fig. 1 of Sarret *et al.*, 2005). Formal oxidation of selenium dramatically enhances the white line and moves the peak 3–6 eV (depending on the oxidation state) higher in energy relative to SeMet. In fact, the enhancement of the white line from oxidized SeMet was dramatic enough to significantly enhance the phasing power of the derivative (Thomazeau *et al.*, 2001). Reducing to metallic selenium also enhances the white line but shifts the peak ~1.5 eV lower in energy (Fig. 1 of Sarret *et al.*, 2005). The only species described by Sarret *et al.* with significantly weaker white-line intensity than SeMet is selenourea. The double bond to carbon is shorter than a single bond, which increases the electron density in the outer orbitals of the selenium atom. The radiation damage product of SeMet had no white line and therefore does not correspond exactly to any of the reference compounds assayed by Sarret *et al.* The damage product could be similar to selenourea, but even selenourea has a small white line. It is not unreasonable to suppose that the radiation damage product of SeMet is a radical, and a methylselenol radical will not have a white line if the 4*p* orbital is completely occupied by the unpaired electron. Unfortunately, there are no stable radical selenium reference compounds with which to test this hypothesis.

Assuming that the change in the height of the white line is caused by the same reaction that leads to disordered Se atoms in the crystal electron density, the implications of these data for the mechanisms of radiation damage in protein crystallography are discussed.

1.3. Energy transfer from X-ray photons to chemistry

When considering the rate of radiation damage to SeMet side chains, it is instructive to calculate the rate at which X-ray photons interact directly with the Se atoms in a sample. It is important to remember that the X-ray fluence Φ (photons/area) that will photoionize half of the Se atoms in a thin sample is independent of the concentration of Se in the sample [Se]. The instantaneous rate of photoionization (ions s^{-1} cm^{-3}) is given by multiplying the tabulated photoionization cross section σ (cm^2 $atom^{-1}$) by [Se] (atoms cm^{-3}), the sample thickness t (cm) and the brightness (photons s^{-1} cm^{-2}). The ionization rate is proportional to [Se], so the ratio of the ionization rate to [Se] is a constant. Since the number of ionizations generated by a given fluence Φ (photons/area) will also be a constant (regardless of how much time it takes to deliver the photons), the ionization rate can be expressed in terms of fluence instead of time. So, the photoionization 'rate' [ions cm^{-3}/(photons cm^{-2})] is given by multiplying the cross section σ (cm^2 $atom^{-1}$) by [Se] (atoms cm^{-3}) and the sample thickness t (cm). If one considers ionized Se atoms to be 'reacted', then the rate of change of unreacted Se is given by

$$\frac{\partial}{\partial \Phi}[\mathrm{Se}] = -\sigma\,[\mathrm{Se}]\,t,$$

and the concentration of 'unreacted' Se after a given fluence (Φ) is

$$[\mathrm{Se}] = [\mathrm{Se}]_0 \exp(-\sigma t\,\Phi),$$

where $[\mathrm{Se}]_0$ is the 'initial concentration' of Se. It follows that the fluence required to ionize half of the Se in a (thin) sample of unit thickness is $\ln(2)/\sigma$, which does not depend on the value of [Se]. For 12680 eV photons, the value of σ is 157 cm^2 g^{-1} (Hubbell, 1982). After converting to convenient units, $\ln(2)/\sigma$ becomes 3.37×10^{11} photons μm^{-2} or 337 photons $Å^{-2}$. A beamline producing a brightness of 4×10^6 photons μm^{-2} s^{-1} would take 24 h to deliver this fluence. Since radiation damage to SeMet has been observed to occur in samples that have experienced far fewer photons than this, it is expected that a mechanism other than direct photoionization of Se is responsible for the damage. The fluence of 12540 eV photons required to ionize half of the Se in a thin sample is 23600 photons $Å^{-2}$, given the cross section of 22.4 cm^2 g^{-1}. This represents one week of shutter-open time on a 4×10^6 photons μm^{-2} s^{-1} beamline. Evidently, the mechanism of specific damage must transfer energy deposited into more concentrated species (such as water) to SeMet.

The total amount of energy transferred to the sample can be calculated using programs like *RADDOSE* (Murray *et al.*, 2004, 2005). This energy is deposited by creating electron–ion pairs in the sample. In the case of 12 keV X-rays interacting with light elements such as carbon and oxygen, nearly all of the energy from the photon is imparted to the electron as kinetic energy. The ionized atom is given very little kinetic energy because of conservation of momentum. The atom is left as an electronically excited ion, which does have potential energy, but very little atomic motion (heat) is introduced into the sample at this point. The high-energy electron travels several hundred nanometers through the sample, giving up energy by ionizing or otherwise exciting the atoms it encounters (Nave & Hill, 2005). Just as with the primary event, these secondary ionizations impart far more potential energy than kinetic energy to the atoms. The kinetic energy remains with the (much less massive) electrons. Only after the electrons have slowed down to energies below the minimum ionization threshold of the atoms in the sample do they start to interact appreciably with rotational, vibrational and translational states (Newton, 1963). In the end, most of the liberated electrons from this shower of ionizations eventually attach themselves to an atom, forming an excited negative ion. Some can be trapped in between atoms as a so-called 'solvated electron', which has a dark blue color that fades in visible light (Box, 1977). This blue color can be seen in some protein crystal samples. In general, the immediate result of ionizing radiation is the promotion of a large number of atoms to electronically excited states. The conversion of the kinetic

energy of the absorbed X-ray photon into chemical potential energy is quite efficient. For example, PIN photodiodes convert nearly all (70–95%) of the energy imparted into the silicon of the 'I' layer into an electric current. Very little heat is produced. The physics of the initial energy deposition in protein crystals is exactly the same.

What happens next in a protein sample depends on the available mechanisms for these excited atoms to return to their ground state. In a pure substance there are not many ways that this can happen. The energy cannot simply dissipate as heat because there are no direct mechanisms for coupling the energy of electronic excited states to vibrational and translational states. An instructive analogy is the physics of scintillators, such as NaI:Tl. An incident X-ray photon generates excited states in the NaI crystal, but more than half of the energy brought in by the photon departs the crystal *via* fluorescence from the thallium atoms, which are present in only a few parts per thousand. This 'focusing' of energy onto the thallium arises because the energy imparted to Na and I ions cannot efficiently escape as heat. Simple relaxation of an excited ion to the ground state would emit an ultraviolet photon. Any such photon is readily absorbed by another Na or I ion because these atoms have allowed transitions at exactly the energy of the photon and are present at high concentration. This results only in a net change in location of the excited state. Although the emission and re-absorption of photons is easy to conceptualize, radiationless energy-transfer mechanisms are much more prevalent in the solid state. Exciton migration and Förster resonance energy transfer (FRET to many biochemists) are examples of radiationless energy-transfer mechanisms. Regardless of the transfer mechanism, the excitation energy moves around in the NaI crystal until it finds a way out: thallium. Thallium is used because its excited state is close to the energy of the mobile excited state in NaI, but it has a very different emission spectrum. The light emitted from thallium is not re-absorbed efficiently because the thallium is at such a low concentration.

So, in a solid substance, energy can efficiently and quickly move about and 'focus' on a dilute species, provided the dilute species has an efficient coupling mechanism to the excitation in the medium. It is important to note that polycrystalline scintillators are less efficient than single-crystal ones. Solar cells made from amorphous silicon, nanocrystalline silicon, polycrystalline silicon and single-crystal silicon are progressively more efficient at converting light into electricity. Defects in the crystal lattice create opportunities for the excited states to give up their energy. By analogy, it is expected that the crystalline nature of the medium containing a protein crystal or a correctly chosen additive species could 'quench' the mobile excitations before they have a chance to damage the protein.

The exact nature and distribution of excited states in the sample, as well as the fate of the energy contained in these excited states, depends on the detailed electronic structure of the material. The available states and the allowed transitions between them must be known. The electronic structure of silicon crystals is well understood: the excited states take the form of 'conduction band' electrons and 'holes' carrying 3.6 eV of energy that migrate quickly through the crystal lattice under the influence of electric fields. Unfortunately, the electronic structure of excited states in pure condensed water is only now being worked out, and an excellent review of this field is presented by Garrett *et al.* (2005). The electronic structure of aqueous solutions, especially aqueous solutions of macromolecules, is far more complex than that of pure water and no quantitative predictive models of electronic behavior in these systems exist.

In the absence of a detailed mechanistic model, one can still apply general principles. The 'resonance principle' dictates that the more closely matched the energy levels of two states, the more probable the transfer of energy between them (Newton, 1963). That is, the transfer of large quanta of energy into low-energy transitions has weak coupling. This is why most high-energy X-ray photons pass right through protein samples, interacting with them only rarely. Note that sample heating by the X-ray beam can be defined as coupling to acoustical phonon states, which have very low energy (0.05 eV). The transfer of energy from X-ray photons into heat will therefore be quite a bit less efficient than the transfer of energy into chemical transformations (around 5 eV), because the latter will have much stronger coupling to high-energy events. In fact, it is most likely that any change in the sample temperature is a result of chemical changes (5 eV coupling to 0.05 eV), and not the other way around. On the other hand, if a particular excited species is present at high concentration (such as water in an aqueous solution) then the transfer of energy from an excited water molecule to nearby unexcited water molecules will be very efficient. It is known that the excited states of water range between 6.6 and 12.6 eV (Garret *et al.*, 2005). This is higher than the 1.14 eV 'band gap' of silicon, which classifies water as an electrical insulator, but excited-state migration through water does occur. In fact, energy deposited into amorphous solid water has been shown to produce chemical changes only at the interfaces between the solid water and vacuum or the support structures, and no chemistry takes place in the bulk (Petrik & Kimmel, 2003). The chemistry under study in this case was the dissociation of water into hydrogen gas, but energy deposited into the bulk cannot dissociate water molecules there because of cage effects. The excited-state energy must migrate to the surface before it finds a water molecule that can dissociate. The transfer of an excitation may or may not include the transfer of a charge, so excited ions and radicals can effectively migrate through the medium without the need for any atomic motions. The questions here then become: what excited states in the sample have the longest lifetimes and what mechanisms are available to couple those states to the breakdown of selenomethionine?

1.4. Factors affecting selenomethionine lifetime

The same chemical species at two different locations in the same crystal has been observed to decay at significantly different rates (Burmeister, 2000; Leiros *et al.*, 2001; Weik *et*

al., 2001; Nukaga *et al.*, 2003; Fuhrmann *et al.*, 2004; Carugo & Carugo, 2005; Dubnovitsky *et al.*, 2005; Roberts *et al.*, 2005; Yano *et al.*, 2005; Leiros *et al.*, 2006). Apparently, the position of a chemical species in the unit cell is related to the damage rate. The mechanism of this differential sensitivity is not clear, but it must be related to the primary or tertiary structure of the molecule and perhaps the arrangement of molecules in the crystal itself. Solvent accessibility is often implicated as having a positive correlation with radiation sensitivity, but clear counterexamples exist. Methionine in particular appears to be more labile when buried in the core (Burmeister, 2000). A better understanding of the mechanisms governing differential sensitivity is important for making a critical evaluation of potentially damaged protein structures.

Admittedly, a better understanding of the structural determinants of differential sensitivity is unlikely to be useful to an experimenter trying to determine the structure in the first place. The protein structure and the structure of the crystal lattice are not generally under the experimenter's control, but any predictive information about the expected lifetime of SeMet side chains would be useful in designing the data collection strategy. There are also a number of factors potentially under the experimenter's control that could influence the lifetime of SeMet. Variation of beam intensity (Leiros *et al.*, 2006), photon energy (Helliwell *et al.*, 1993; Gonzalez *et al.*, 1994, 2005), temperature (Weik *et al.*, 2001, 2005), selenium concentration, pH or cryoprotectant choice as well as the introduction of radioprotective additives such as ascorbate (Murray & Garman, 2002) can all be attempted. The nitrate ion, like ascorbate, is a good electron acceptor and has been used as an electron scavenger in low-temperature ESR (electron spin resonance) studies for some time (Box, 1977). Mobile electrons react with a nitrate ion and convert it into a nitrite ion. Nitrate and ascorbate both have the additional advantage of having a low average atomic number, so the addition of these reagents as 'radioprotectants' will not have the undesirable effect of increasing the total absorption of X-rays by the sample.

The work described here quantifies the influence of sample preparation, temperature, photon energy, selenium concentration, pH, chemical additives and protein structure on SeMet lifetime using XANES as a probe for the progression of the SeMet radiation damage reaction.

2. Methods

2.1. Sample preparation

All measurements reported here were made at the protein crystallography beamlines 8.3.1 or 12.3.1 at the Advanced Light Source (ALS) (MacDowell *et al.*, 2004). The exact composition of each sample is described in Table 1. Most of these samples were prepared with a SeMet concentration of 25 or 31 m*M*. This concentration range was chosen because it is on the low end of the SeMet content found in protein crystals. A crystal containing 50% solvent and one SeMet in 200 amino acid residues will be 25 m*M* Se. This ratio of Se to amino acids represents a challenging structure solution problem because long data collection times are required to measure weak anomalous signals and the length of data collection is ultimately limited by radiation damage. Knowledge of radiation damage at low Se concentration is expected to be most relevant to such projects.

Unless otherwise noted, the cosolvent ('cryoprotectant') used to aid flash-cooled vitrification was 25% (*v*/*v*) glycerol. Unless an acidic or basic additive was being tested, 50 m*M* bis-tris (unbuffered) was used to keep the free amino acid of SeMet soluble (and not always indicated in Table 1). For a typical experiment, a 2–3 nL droplet of each solution was mounted in a 0.3–0.4 mm nylon crystal mounting loop (Hampton Research) and flash-cooled in liquid nitrogen. Once mounted on the beamline, the samples were photographed and the dimensions of the droplet measured using the calibrated pixel size of the beamline microscope. The measured thicknesses traversed by the X-ray beam through each sample are listed in Table 1.

Trigonal crystals of GCN4-N16A-p1 peptide (GCN4) were chosen for this study because of the unusually long lifetime observed for both the diffraction strength and the electron density of the SeMet side chains. These crystals were grown as described previously [Holton & Alber, 2004; Protein Data Bank (PDB) ID 1RB5]. The crystal dimensions were 70 µm × 70 µm × 70 µm (droplet 31 in Table 1) and 70 µm × 70 µm × 100 µm (droplet 32). The structure has three Se atoms per asymmetric unit, which corresponds to a Se concentration of 92.6 m*M*. Each crystal was soaked for 1 h in cryoprotectant [100 m*M* bis-tris pH 7.3 with 15% (*v*/*v*) MPD (2-methyl-2,4-pentanediol) and 5% (*w*/*v*) PEG8K] before being flash-cooed in liquid nitrogen.

Crystals containing the E1 domain of NEDD8 (NE1) were kindly provided by Brenda Schulman. The structure of this domain is known (Huang *et al.*, 2004; PDB ID 1Y8X), but the crystals used here were of a Leu394Met mutant that crystallized in a new and currently unsolved form. These crystals contained 31 m*M* Se and were soaked for 15 min in cryoprotectant (0.9 *M* sodium citrate, 0.2 *M* sodium chloride, 0.1 *M* Tris-HCl pH 7.6, 30% glycerol) before being flash-cooled in liquid nitrogen. These crystals were solicited for this study because the first attempt to solve this crystal form by MAD failed despite an apparently strong anomalous signal, and it was suspected that these crystals contained radiation-sensitive side chains. The NE1 crystal (droplet 29) was 50 µm × 60 µm × 280 µm, so all crystal dimensions were larger than the 'probe beam' used to assay SeMet integrity.

During data collection all samples were cooled by an Oxford Instruments CryoJet (Oxford Instruments, UK) oriented with the gas stream coaxial with the sample pin. A droplet of 2-methylbutane, mounted in a sample loop, melted when the commanded sample temperature reached 111.7 K. Since 2-methylbutane is known to melt at 113 ± 1 K (Forziati *et al.*, 1946; Howard *et al.*, 1947), the sample temperature in these experiments was assumed to be roughly 1 K above the displayed temperature of the CryoJet stream.

2.2. Exposure control

The data collection procedure alternated between using a collimated and highly attenuated (100–200-fold) 'probe beam' to collect XANES data (referred to here as an XANES session) interspersed with exposing the sample to unattenuated and uncollimated 'dosing beam' for controlled periods of time (a 'burn'). Unless otherwise noted, the 'burn' was conducted at 12680 eV. The 'dosing beam' was delivered to the sample for 12–20 s at a time, interspersed by 'dark' intervals of 1 s to 700 s or more. The 'dark' intervals served different purposes. Each shutter-open interval was followed by closing the shutter for 1 s to allow the beam feedback system described by MacDowell *et al.* (2004) to engage and ensure that the beam did not drift during the 'burn'. Long protein crystallography (PX) exposures at beamlines 8.3.1 and 12.3.1 use a similar shutter control protocol. The overhead of switching to the 'probe beam', collecting an XANES session and switching back to the 'dosing beam' averaged 665 ± 184 s. Storage-ring refills or unexpected beam dumps could introduce delays from 15 min to up to 5 h. This dose delivery schedule was not unlike that experienced by a PX sample during ordinary data collection. Unlike a PX sample, these samples were not rotated during data collection, which simplifies the dose calculations.

The shutter-open time varied from 12 to 20 s in order to match a prescribed dose delivery schedule. The total shutter-open time between the first and second XANES session of each run was 30 s (the first 'burn'). The total shutter-open time between subsequent XANES sessions was increased by a factor of 1.2 for each subsequent 'burn' until it reached 600 s at the 18th 'burn' and beyond. This geometrically increasing 'burn' duration allowed the same data collection script and data analysis procedure to be used to measure the wide range of decay rates observed. For example, the fastest decay curve measured was halfway to completion after 500 s of shutter-open time. Using a 'burn' duration of more than 50 s would have seriously under-sampled the shape of this decay curve. However, the longest decay curve measured here took 10 h of shutter-open time to collect out to five half-lives. With a 30 s 'burn' interval and average 665 s XANES overhead, this data set would have taken ten days of continuous beam time to collect, and no such blocks of time were available. These time constraints required that XANES sessions be made less often as the total exposure increased.

The final beam-defining aperture used here was either a 30 μm or 100 μm round pinhole in a 50 μm-thick tantalum foil (National Aperture, Salem NH). The pinhole was placed 12 mm up-beam from the sample position for brightness measurements and XANES sessions, but it was removed during each 'burn' to minimize the impact of sample drift. Using the uncollimated beam (no pinhole) for each 'burn' provided even illumination over an area of sample that was larger than the region probed by XANES. Performing the 'burn' in this way eliminated the systematic errors that would be introduced if the 'burnt' part of the sample were the same size as the pinhole and drifting in and out of the beam during XANES.

After the 'burn', the pinhole was inserted and the 'dosing beam' brightness (photons/area/time) was measured (described below). After the brightness measurement, the beam through the pinhole was attenuated for an XANES session (the 'probe beam'). The magnitude of this attenuation was optimized for each sample at the beginning of the run. An Al attenuator foil was inserted and the upstream horizontal divergence slits were closed to 0.1 mrad, which attenuates the beam by a factor of 130. The slits were then slowly opened until $\sim$90000 counts s^{-1} registered on the XANES detector. For a typical sample thickness of 180 μm, this was achieved at 37-fold attenuation. These optimal attenuation settings were then saved and re-applied for each XANES session. If the mean counts s^{-1} measured during the XANES session deviated by more than 5% from 90000, the horizontal divergence slits were adjusted to compensate. This minimized the nonlinearity introduced by pulse overlap in the XANES detector. After the XANES session the attenuation was removed, the beam was re-optimized to maximize the flux through the pinhole and then the 'dosing beam' brightness was measured again. After this 'pre-burn' brightness measurement, a 60 s X-ray diffraction pattern was recorded from the sample using the unattenuated beam through the pinhole. This was the only time that the sample experienced unattenuated beam through the pinhole. After the diffraction pattern was recorded, the collimating pinhole was removed in order to begin the next 'burn'.

2.3. X-ray diffraction

Diffraction patterns at ALS 8.3.1 were made with an Area Detector Systems Quantum 210 area detector (Poway, CA, USA). Diffraction measurements at ALS 12.3.1 used a Quantum 315 detector from the same vendor. Each 60 s diffraction pattern recorded from the sample was accompanied by an additional 60 s diffraction pattern taken with the sample temporarily driven out of the beam path. This second pattern was subtracted from the diffraction pattern of the sample to remove air scatter and other instrument background. The difference image was circularly integrated and corrected for Lorentz and polarization effects using the program *FIT2D* (Andy Hammersley, ESRF). The diffraction signal was then corrected for air absorption and detector gain and normalized to photons $sterad^{-1}$ plotted against $4\sin(\theta)/\lambda$. Diffraction patterns from the protein crystal samples were subjected to the same circular integration method. The contribution from Bragg peaks appeared as noise but the overall pattern was clear enough to assign the amorphous/nanocrystalline character of the cryoprotectant.

The diffraction patterns fell into three main categories: an amorphous solid, nanocrystalline cubic ice and a mixture of the two. The nanocrystalline cubic ice is described in detail in §3.3.2 and is referred to here as 'nano-ice'. The ratio of the components of the mixture was quantitated by fitting the

diffraction pattern of each sample to a linear combination of two reference diffraction patterns. Reference patterns were generated by averaging the diffraction patterns from samples selected by hand as representative of each state. Droplets 46, 50, 57, 130 and 131 were selected to represent nanocrystalline cubic ice. The diffraction data from the 30 samples now listed in Table 1 as being less than 5% nanocrystalline were averaged to represent the amorphous state. The relative contribution of each substance to the diffraction pattern of each sample was quantified by least-squares fitting a linear combination of the two reference patterns and a smooth quadratic baseline to the observed diffraction pattern of each sample. The baseline was included to account for the differing amounts of fluorescence from the samples, which was also picked up by the area detector.

It is noteworthy that the '%nano-ice' parameter reported in Table 1 stayed close to a physically reasonable interval (0–100%) for most of the fit results. The fitting procedure put no constraint on the '%nano-ice' number reported in Table 1. For this reason some of the values in Table 1 are greater than 100% and some are slightly negative. These small deviations are most likely due to noise and the unknown relative scale of the two reference patterns. Not every diffraction pattern could be explained as a linear combination of the two references. For example, the fits to the diffraction pattern from samples containing 9.5 *M* urea both converged to −30% nano-ice. These patterns contain broad lines similar to those in the amorphous reference pattern, but the low-angle peak from the urea-containing samples was stronger relative to the second peak. The fit procedure converged on a solution that subtracted the nano-ice pattern from the amorphous pattern to compensate. It was concluded that the urea must be altering the water structure in these samples in a way not represented by the reference patterns. For this reason, samples that produced broad diffraction rings but did not fit the reference diffraction pattern are listed as 'amrph' in Table 1. Likewise, diffraction patterns that contained the sharp rings of a crystalline substance (such as hexagonal ice) are indicated explicitly. The '%nano-ice' numbers indicate samples that produced diffraction patterns that were in good agreement with a linear combination of the two reference patterns and serve to quantitate what would otherwise be a subjective interpretation.

2.4. XANES measurements

XANES measurements at ALS 8.3.1 were made using a NaI:Tl scintillator (Oxford Danfysik model CBY38NA01B) connected to a single-channel analyzer (Oxford Danfysik model CyberStar X1000). Although the energy-resolving power of this detector is poor and scattered photons could not be discriminated from fluorescent photons, the large active area of this detector (3 cm diameter) measures a large number of total counts per unit of incident fluence onto the sample. Therefore, a good signal-to-noise ratio is achieved in the XANES spectrum with minimal dose to the sample.

XANES measurements at ALS 12.3.1 were made using an Evex SDD detector (Princeton, NJ) with 128 eV energy resolution connected to a Canberra DSA-1000 multi-channel analyzer (Connecticut). This detector discriminated fluorescent photons from scattered photons, but had a smaller active area than the NaI:Tl scintillator. The lower count rate per incident photon of this set-up was compensated for by the higher signal-to-noise provided by energy discrimination. The dose delivered to the sample during XANES measurements on both beamlines was comparable.

Full XANES spectra were collected at the beginning of each run in order to locate the top of the white-line peak and verify that there were no unusual features in the SeMet XANES (such as evidence of oxidation during sample preparation). A full XANES spectrum was also taken after every 20th 'burn' (approximately every 30 MGy). Since the acquisition of full XANES spectra was time-consuming (600 s each) and beam time was limited, the XANES sessions were limited to ten critical excitation energies. Three energies in the 'low' baseline (12490, 12515 and 12540 eV), three energies in the 'high' baseline (12700, 12725 and 12750 eV), the 'peak' at the apex of the 'white line' feature (∼12657 eV), 0.4 eV below the peak, 0.4 eV above the peak and 2.0 eV above the peak ('valley') were selected to represent the full spectrum. All ten energy points were collected as a set. This set of ten measurements was repeated up to 50 times or until the mean difference between the peak and high remote data was greater than 30 times the scatter in that difference. Once one of these conditions was met, all counts taken at a given energy were summed together to minimize the influence of any intensity drift during the XANES session. To minimize the influence of scattered photons in the baseline, the height of the white-line peak was normalized to the cross section by scaling the photon counts so that the 'high' and 'low' measurements took on the known cross section of Se values at those energies: 156 and 22.4 $cm^2\ g^{-1}$, respectively (Hubbell, 1982). The cross section at the peak was inferred from this scale.

2.5. Peak lock

To ensure that the observed changes in the 'peak' fluorescence intensity were due to changes in the white-line peak height and not due to monochromator drift, the position of the 'peak' of each sample was monitored and followed throughout the run. The XANES at the beamlines used was smooth with respect to changes in energy smaller than ∼1.8 eV [the bandpass of a Si(111) monochromator at 12660 eV] because XANES spectra are convoluted with the energy spread in the photon beam. Therefore, any two points in the spectrum closer than ∼0.5 eV can be treated as a straight line corrupted by photon-counting noise. The top of any peak is therefore 'flat' on this scale. This allowed the use of a simple algorithm to track the photon-energy setting that corresponded to the top of the while-line peak. If the number of counts 0.4 eV above and 0.4 eV below the maximum were not equal, then the next commanded 'peak' energy was updated by 0.01 eV in the appropriate direction. This damped peak lock algorithm was

Table 1
Details of the individual decay rate measurements.

An ordinal serial number was assigned to each sample (droplet) when it was prepared and flash-cooled in liquid nitrogen. The experiments are listed here in chronological order. Pairs of samples used to calculate protection factors were collected as close together as possible in time and so this chronological listing is most efficient at listing compared droplets side-by-side. The half-reaction dose ($D_{\frac{1}{2}}$) derived from a single-exponential fit to the peak cross-section measurements against dose is provided along with the propagated standard error of that fit. The extent of the high-dose baseline available in the curve fit is indicated by the number of times a dose equivalent to $D_{\frac{1}{2}}$ had been delivered to the sample by the end of the run. The total concentration of Se in any form is listed, followed by the nature of the selenium-containing species: the free SeMet amino acid, a peptide or a crystal. Other components of the sample are listed under 'Notes'. The thickness of each sample was measured optically with the beamline microscope. The physical state of the sample was evaluated by comparing the diffraction pattern to reference patterns as described in the text. A score of 100% indicates the pattern exactly matched the one described for nano-ice; a score of 0% indicates that the pattern exactly matched that of amorphous solid water. Amorphous samples that did not fit a linear combination of these two patterns well, but had broad diffraction rings, are indicated as 'amrph'; unk = unknown. Other phases, such as ice Ih, are indicated explicitly. The sector number of the beamline used to collect the data is indicated '8' meaning ALS 8.3.1 and '12' meaning ALS 12.3.1. The size of the pinhole and the photon energy used to dose the sample, as well as the dose rate, are provided.

Droplet number	Date of data collection	$D_{\frac{1}{2}}$ half-dose (MGy)	$xD_{\frac{1}{2}}$ (end of run)	[Se] (m*M*)	Se-containing species	Sample thickness (mm)	Physical state of sample (%nano-ice)	Temp. (K)	Beamline sector	Pinhole (μm)	Incident photon energy (eV)	Dose rate (kGy s^{-1})	Notes
17	Nov 11 05	9.77 ± 0.3	8	25	SeMet	0.157	unk	92	8	100	12540	5–9	50 m*M* bis-tris 25% glycerol
19	Nov 13 05	12.1 ± 0.71	5	25	SeMet	0.132	unk	92	8	100	12680	5–9	50 m*M* bis-tris 25% glycerol
20	Nov 15 05	22 ± 1.2	4	25	SeMet	0.090	unk	92	8	100	12680	5–9	800 m*M* ascorbic acid 25% glycerol
21	Nov 16 05	14.8 ± 0.5	6	25	SeMet	0.156	unk	92	8	100	12680	6–9	1 *M* acetic acid 25% glycerol
25	Nov 22 05	31.1 ± 1.1	3	25	SeMet	0.123	unk	92	8	100	12680	4–8	1 *M* HNO_3 25% glycerol
29	Dec 07 05	10.9 ± 3	4	33	Xtal	0.058	unk	92	8	100	12680	5–9	NE1 #3
30	Dec 08 05	9.54 ± 0.87	4	25	SeMet	0.117	unk	92	8	100	12540	6–8	50 m*M* bis-tris 25% glycerol
31	Dec 10 05	31.8 ± 0.76	7	93	Xtal	0.068	amrph	92	8	100	12540	3–12	GCN4-p1-N16A 2 $P3_121$ 100 m*M* bis-tris pH = 8 15% MPD 5% PEG8K
32	Dec 14 05	43.2 ± 2	5	93	Xtal	0.080	101%	92	8	100	12680	6–10	GCN4-p1-N16A 3 $P3_121$ 100 m*M* bis-tris pH = 8 15% MPD 5% PEG8K
34	Dec 19 05	14.2 ± 0.56	6	25	SeMet	0.117	65%	92	8	100	12680	5–9	100 m*M* bis-tris 15% MPD 5% PEG8K
38	Jan 28 06	16.9 ± 0.53	10	25	SeMet	0.106	5%	92	8	100	12680	7–12	50 m*M* bis-tris 25% glycerol
39	Jan 30 06	16.8 ± 0.76	4	25	SeMet	0.223	−1%	92	8	100	12680	7–10	50 m*M* bis-tris 25% glycerol 1 *M* acetic acid
40	Jan 31 06	16.4 ± 0.28	9	25	SeMet	0.119	5%	92	8	100	12680	6–10	50 m*M* bis-tris 25% glycerol
43	Feb 07 06	38.9 ± 1.3	4	25	Peptide	0.158	3%	92	8	100	12680	6–11	GCN4-N16A-p1 100 g/L pure 450 m*M* acetic acid 25% glycerol 5 m*M* EDTA
44	Feb 04 06	17.3 ± 0.74	6	25	SeMet	0.166	49%	92	12	100	12680	5–9	50 m*M* bis-tris 25% glycerol
45	Feb 07 06	5.61 ± 0.51	7	4	SeMet	0.281	unk	92	12	100	12680	3–7	0.6 *M* NaOH 25% glycerol
46	Feb 08 06	11.8 ± 0.33	11	62	SeMet	0.181	88%	92	12	100	12680	7–13	0.6 *M* NaOH 25% glycerol
47	Feb 09 06	11.6 ± 0.53	8	125	SeMet	0.107	−3%	92	8	100	12680	8–14	0.6 *M* NaOH 25% glycerol
48	Feb 11 06	16.1 ± 0.51	13	25	SeMet	0.177	53%	92	12	100	12680	4–12	50 m*M* bis-tris 25% glycerol
49	Feb 16 06	11.8 ± 0.38	17	500	SeMet	0.089	−8%	92	8	100	12680	13–25	0.6 *M* NaOH 25% glycerol
50	Feb 18 06	9.69 ± 0.94	4	8	SeMet	0.265	105%	92	8	100	12680	6–10	0.6 *M* NaOH 25% glycerol

Table 1 (continued)

Droplet number	Date of data collection	$D_{\frac{1}{2}}$ half-dose (MGy)	$xD_{\frac{1}{2}}$ (end of run)	[Se] (m*M*)	Se-containing species	Sample thickness (mm)	Physical state of sample (%nano-ice)	Temp. (K)	Beamline sector	Pinhole (μm)	Incident photon energy (eV)	Dose rate (kGy s^{-1})	Notes
52	Feb 23 06	12.9 ± 0.4	6	31	SeMet	0.130	34%	92	8	100	12680	6–11	0.6 *M* NaOH 25% glycerol
53	Feb 24 06	30.5 ± 2.4	6	25	Peptide	0.082	3%	92	8	100	12680	6–11	GCN4-N16A-p1 100 g/L pure 450 m*M* acetic acid 25% glycerol 5 m*M* EDTA
55	Feb 26 06	12.6 ± 0.31	8	62	SeMet	0.107	2%	92	8	100	12680	7–13	0.6 *M* NaOH 25% glycerol
56	Feb 26 06	6.66 ± 0.45	23	8	SeMet	0.128	18%	92	12	100	12680	6–12	0.6 *M* NaOH 25% glycerol
57	Mar 01 06	5.98 ± 0.22	5	16	SeMet	0.161	106%	92	8	100	12680	5–13	0.6 *M* NaOH 25% glycerol
59	Mar 02 06	11.8 ± 0.36	7	16	SeMet	0.164	−6%	92	12	100	12680	5–8	0.6 *M* NaOH 25% glycerol
63	Mar 31 06	32.1 ± 0.69	6	25	Peptide	0.219	−1%	92	8	100	12680	5–11	GCN4-N16A-p1 100 g/L pure 450 m*M* acetic acid 25% glycerol 5 m*M* EDTA 40% sat urea
64	Mar 31 06	8.13 ± 0.16	14	31	SeMet	0.272	109%	92	12	100	12680	6–12	0.6 *M* NaOH 25% glycerol
65	Apr 01 06	10.9 ± 0.45	5	31	SeMet	0.229	95%	92	12	100	12680	7–10	0.6 *M* NaOH 25% glycerol
66	Apr 01 06	15.8 ± 0.59	7	20	Peptide	0.281	amrph	92	8	100	12680	6–11	GCN4-N16A-p1 80 g/L pure 9.5 *M* urea
67	Apr 02 06	13.7 ± 0.58	19	20	Peptide	0.328	amrph	92	12	100	12680	6–13	GCN4-N16A-p1 80 g/L pure 9.5 *M* urea
68	Apr 05 06	10.6 ± 0.26	12	20	SeMet	0.310	amrph	92	8	100	12680	5–11	80 g/L insulin 9.5 *M* urea
69	Apr 07 06	9.77 ± 0.31	14	16	SeMet	0.157	99%	92	12	100	12680	4–10	0.6 *M* NaOH 25% glycerol
70	Apr 08 06	12.8 ± 0.41	10	16	SeMet	0.281	51%	92	8	100	12680	5–11	0.6 *M* NaOH 25% glycerol
71	Apr 08 06	10.1 ± 0.26	9	31	SeMet	0.231	82%	92	12	100	12680	5–9	0.6 *M* NaOH 25% glycerol
72	Apr 08 06	13.3 ± 0.24	4	31	SeMet	0.251	35%	92	8	100	12680	6–11	0.6 *M* NaOH 25% glycerol
73	Apr 09 06	12.1 ± 0.31	8	31	SeMet	0.328	−6%	92	12	100	12680	5–9	0.6 *M* NaOH 25% glycerol
74	Apr 19 06	12.8 ± 0.32	5	31	SeMet	0.145	5%	92	8	100	12680	5–9	0.6 *M* NaOH 25% glycerol
77	Apr 20 06	14.6 ± 0.48	7	31	SeMet	0.149	10%	92	12	100	12680	6–12	0.6 *M* NaOH 25% glycerol
78	Apr 25 06	13.5 ± 0.52	8	31	SeMet	0.066	−9%	92	12	100	12680	6–11	0.6 *M* NaOH 25% glycerol
79	Apr 26 06	14.5 ± 0.81	6	31	SeMet	0.176	2%	92	12	100	12680	6–14	0.6 *M* NaOH 25% glycerol
80	Apr 27 06	14.5 ± 0.66	9	31	SeMet	0.196	0%	92	12	100	12680	6–11	0.6 *M* NaOH 25% glycerol
81	Apr 28 06	14.4 ± 0.53	7	31	SeMet	0.175	6%	92	12	100	12680	5–10	0.6 *M* NaOH 25% glycerol
82	Apr 29 06	14.5 ± 0.55	9	31	SeMet	0.191	−4%	130	12	100	12680	4–8	0.6 *M* NaOH 25% glycerol
84	May 05 06	25.1 ± 1.1	7	25	Peptide	0.174	5%	140	8	100	12680	5–9	GCN4-N16A-p1 100 g/L pure 450 m*M* acetic acid 25% glycerol 5 m*M* EDTA
85	May 09 06	11.1 ± 0.47	4	31	SeMet	0.169	1%	92	8	100	12680	5–7	0.6 *M* NaOH 25% glycerol

Table 1 (continued)

Droplet number	Date of data collection	$D_{\frac{1}{2}}$ half-dose (MGy)	$xD_{\frac{1}{2}}$ (end of run)	[Se] (m*M*)	Se-containing species	Sample thickness (mm)	Physical state of sample (%nano-ice)	Temp. (K)	Beamline sector	Pinhole (μm)	Incident photon energy (eV)	Dose rate (kGy s^{-1})	Notes
86	May 10 06	7.97 ± 0.37	6	31	SeMet	0.161	12%	140	8	100	12680	5–9	0.6 *M* NaOH 25% glycerol
87	May 13 06	9.67 ± 0.29	9	31	SeMet	0.139	7%	130	8	100	12680	5–9	0.6 *M* NaOH 25% glycerol
88	May 13 06	12.3 ± 0.32	7	31	SeMet	0.173	0%	92	8	100	12680	5–10	0.6 *M* NaOH 25% glycerol
89	May 13 06	12.5 ± 0.33	6	31	SeMet	0.147	2%	92	8	100	12680	5–9	0.6 *M* NaOH 25% glycerol
90	May 15 06	13.3 ± 0.24	8	31	SeMet	0.183	5%	93	8	100	12680	5–9	0.6 *M* NaOH 25% glycerol
91	May 15 06	16.4 ± 0.64	9	31	SeMet	0.157	10%	93	12	100	12680	6–12	0.6 *M* NaOH 25% glycerol
92	May 16 06	10.8 ± 0.29	9	31	SeMet	0.146	7%	110	8	100	12680	5–9	0.6 *M* NaOH 25% glycerol
93	May 16 06	12.8 ± 0.56	11	31	SeMet	0.177	18%	93	12	100	12680	5–11	0.6 *M* NaOH 25% glycerol
94	May 18 06	9.61 ± 0.35	9	31	SeMet	0.172	7%	130	8	100	12680	5–9	0.6 *M* NaOH 25% glycerol
95	May 17 06	15.6 ± 0.69	8	31	SeMet	0.146	−3%	93	12	100	12680	5–10	0.6 *M* NaOH 25% glycerol
97	May 18 06	11.9 ± 0.77	6	31	SeMet	0.162	5%	93	12	100	12680	4–8	0.6 *M* NaOH 25% glycerol
98	May 19 06	13.3 ± 0.47	6	31	SeMet	0.011	5%	93	12	100	12680	6–12	0.6 *M* NaOH 25% glycerol
99	May 25 06	13.8 ± 0.59	8	31	SeMet	0.175	5%	93	12	100	12680	7–11	0.6 *M* NaOH 25% glycerol
100	May 22 06	5.27 ± 0.14	11	31	SeMet	0.171	51%	155	8	100	12680	5–9	0.6 *M* NaOH 25% glycerol
101	May 23 06	12 ± 0.46	4	31	SeMet	0.163	1%	93	8	100	12680	5–8	0.6 *M* NaOH 25% glycerol
102	May 25 06	13.3 ± 0.25	11	31	SeMet	0.163	0%	93	8	100	12680	5–10	0.6 *M* NaOH 25% glycerol
103	May 26 06	13.3 ± 0.31	6	31	SeMet	0.133	−1%	93	8	100	12680	6–9	0.6 *M* NaOH 25% glycerol
104	May 26 06	13 ± 0.25	11	31	SeMet	0.122	−1%	93	8	100	12680	6–10	0.6 *M* NaOH 25% glycerol
105	May 27 06	14.5 ± 0.51	16	31	SeMet	0.127	2%	93	12	100	12680	6–11	0.6 *M* NaOH 25% glycerol
106	May 28 06	10.4 ± 0.27	10	31	SeMet	0.166	−2%	120	8	100	12680	5–9	0.6 *M* NaOH 25% glycerol
107	Jun 01 06	12.2 ± 0.34	5	31	SeMet	0.156	−2%	93	8	100	12680	4.5	0.6 *M* NaOH 25% glycerol
108	Jun 02 06	13.1 ± 0.58	9	31	SeMet	0.118	−4%	93	12	100	12680	4.5	0.6 *M* NaOH 25% glycerol
110	Jun 03 06	5.09 ± 0.16	24	31	SeMet	0.181	iceIh	93	12	100	12680	4.5	0.6 *M* NaOH 25% glycerol ice
111	Jun 06 06	13 ± 0.33	15	31	SeMet	0.160	−1%	93	12	100	12680	4.5	0.6 *M* NaOH 25% glycerol
112	Jun 11 06	15.9 ± 1	2	31	SeMet	0.171	−1%	93	8	100	12680	4.5	0.6 *M* NaOH 25% glycerol
113	Jun 14 06	12.3 ± 0.21	11	31	SeMet	0.166	1%	93	8	100	12680	4.5	0.6 *M* NaOH 25% glycerol
114	Jul 03 06	11.8 ± 0.17	16	31	SeMet	0.172	1%	93	8	100	12680	4.5	0.6 *M* NaOH 25% glycerol
115	Jul 05 06	12.4 ± 0.23	13	31	SeMet	0.191	3%	93	8	100	12680	4.5	0.6 *M* NaOH 25% glycerol
116	Jul 05 06	12.9 ± 0.32	29	31	SeMet	0.151	4%	93	12	100	12680	4.5	0.6 *M* NaOH 25% glycerol
117	Jul 08 06	10.1 ± 1.8	1	31	SeMet	0.171	1%	93	8	100	12680	4.5	0.6 *M* NaOH 25% glycerol
118	Jul 10 06	12.4 ± 1.3	5	31	SeMet	0.166	−2%	93	12	100	12680	4.5	0.6 *M* NaOH 25% glycerol
120	Jul 11 06	11.6 ± 0.2	10	31	SeMet	0.171	−9%	93	8	100	12680	4.5	0.6 *M* NaOH 25% glycerol
121	Jul 14 06	11.6 ± 0.28	8	31	SeMet	0.181	2%	93	8	100	12680	4.5	0.6 *M* NaOH 25% glycerol
122	Aug 05 06	10.8 ± 0.29	4	31	SeMet	0.182	−5%	93	8	100	12680	4.5	0.6 *M* NaOH 25% glycerol

Table 1 (continued)

Droplet number	Date of data collection	$D_{\frac{1}{2}}$ half-dose (MGy)	$xD_{\frac{1}{2}}$ (end of run)	[Se] (m*M*)	Se-containing species	Sample thickness (mm)	Physical state of sample (%nano-ice)	Temp. (K)	Beamline sector	Pinhole (μm)	Incident photon energy (eV)	Dose rate (kGy s^{-1})	Notes
124	Aug 06 06	13.1 ± 0.45	6	31	SeMet	0.179	3%	93	12	100	12680	4.5	0.6 *M* NaOH 25% glycerol
125	Sep 01 06	12.5 ± 0.24	10	31	SeMet	0.177	2%	93	8	100	12680	4.5	0.6 *M* NaOH 25% glycerol
126	Sep 10 06	12.4 ± 0.48	5	31	SeMet	0.150	1%	93	12	100	12680	4.5	0.6 *M* NaOH 25% glycerol
127	Sep 16 06	14.1 ± 0.56	10	31	SeMet	0.185	3%	93	8	100	12680	4.5	0.6 *M* NaOH 25% glycerol
128	Sep 19 06	13.3 ± 0.25	9	31	SeMet	0.198	−2%	93	8	100	12540	4.5	0.6 *M* NaOH 25% glycerol
129	Sep 20 06	12.3 ± 0.46	4	31	SeMet	0.186	−6%	93	8	100	12680	4.5	0.6 *M* NaOH 25% glycerol
130	Sep 26 06	8.48 ± 0.28	12	31	SeMet	0.246	99%	93	8	100	12680	4.5	0.6 *M* NaOH 25% glycerol
131	Oct 06 06	7.53 ± 0.28	3	31	SeMet	0.207	98%	93	8	100	12680	4.5	0.6 *M* NaOH 25% glycerol

found to be stable until near the end of the run when the 'white line' disappears. For this reason the commanded peak energy was constrained to be within 0.5 eV of the average value of the maximum peak position for the entire run. This tended to keep the expected peak energy in the neighborhood of the original peak position after the white line was gone. In practice, the photon energy of the selenium white-line peak was found to drift about with mean amplitude of 0.1 eV and a timescale of about 20 min. It is assumed that this drift is due to instabilities in the monochromator and not some kind of random chemical fluctuation in the sample.

2.6. Sample and beam alignment

Movement of the sample relative to the beam over the long timescale (12–36 h) of these experiments was combated by automatically re-aligning the loop using a reference image of the sample taken at the beginning of the run. Periodically, a digital image of the microscope field of view was taken and translated over the reference image until the correlation coefficient of the two images was maximized. The appropriate translation of the sample to restore its original appearance in the microscope field of view was then automatically applied. The average correction in the commanded sample position applied by this automatic re-alignment was 5 μm r.m.s. over all these runs.

The alignment of the pinhole with the microscope field of view is quite stable at ALS beamlines 8.3.1 and 12.3.1 (MacDowell *et al.*, 2004). The image of the X-ray beam on a phosphor in the microscope field of view is checked daily and it has not moved by more than a few μm over the past several years. Since the sample was being actively stabilized in the microscope field of view it was effectively being aligned with the pinhole as well. The X-ray beam was also being periodically aligned to the pinhole by optimizing the flux through the pinhole before each 'burn'. Therefore the alignment of the X-ray beam with the sample was stable to within about 5 μm.

2.7. Dose calculation

X-ray doses are given here in mega-Gray (MGy) which is defined as 10^6 J kg^{-1} of absorbed energy. Dose calculations were performed using the program *RADDOSE* (Murray *et al.*, 2004, 2005). For solution samples, the 'solvent content' was set to 100% and the calculation run including the correct heavy-atom content for the solution as usual. However, for experiments where the 'burn' was conducted above the Se *K* edge, some of the energy absorbed by Se atoms left the sample by re-emission as X-ray fluorescence. This fact is not yet taken into account by *RADDOSE* (Murray *et al.*, 2004). The 'mass energy absorption cross section' (μ_{en}/ρ) takes such energy-loss processes into account (Higgins *et al.*, 1992). The μ_{en}/ρ of Se at 12680 eV is 86 cm^2 g^{-1}, and the photoelectric cross section of Se at 12680 eV is 157 cm^2 g^{-1} (Hubbell, 1982). The ratio between these numbers implies that only 54.8% of the energy absorbed by Se remains in the sample. For this reason, all Se concentrations were corrected by 0.548 before providing them to *RADDOSE* when computing doses at 12680 eV.

The brightness (photons/area/time) of the X-ray beam is needed to calculate dose. The brightness was inferred by measuring the photon flux through the pinhole. The flux was measured before and after each 'burn' (described above) and the flux during the 'burn' was interpolated from these values. Dividing the flux (photons s^{-1}) by the aperture area (mm^2) yielded the average brightness (photons s^{-1} mm^{-2}). Multiplying the brightness by the duration of the exposure (s) yields the average fluence (photons mm^{-2}). The average dose delivered to the sample will depend on its atomic composition and to a lesser extent on the sample thickness. Nevertheless, the dose will be directly proportional to the fluence, and the ratio between dose and fluence is given by *RADDOSE* (Murray *et al.*, 2004).

Variation of the beam brightness across the pinhole does not change the average dose delivered to the sample. However, variation of beam brightness across the pinhole does change the 'effective' dose delivered to the sample

because the profile of the 'probe beam' represents a 'weighting function' across the surface of the sample. For example, consider the extreme case of two beams with diameters much smaller than the pinhole and one beam ten times brighter than the other and impacting two different parts of the sample. Essentially, there are two samples in this set-up: one under each beam. The material under the bright beam will be damaged ten times faster than the material under the weak beam. This still does not change the average dose (absorbed energy per unit mass). However, the material under the bright beam will 'count' ten times more than the material under the weak beam during the XANES session because it will also produce ten times more fluorescent photons than the material under the weak beam. The observed decay curve will contain two exponentials with a tenfold difference between their rate constants because the material under the weak beam will have decayed 6.7% at the point in time when the material under the bright beam has already half decayed. Normalizing for this effect required integrating the decay reaction over the shape of the beam profile. This was done by conducting a numerical simulation of the experiment considering every square micrometer of the sample as a separate sample and extracting the 'true' decay rate (that would be observed with perfectly even illumination) from the observed decay curve. This integral required that the beam profile be known.

Prior to these experiments, the profile of the uncollimated X-ray beam focus at ALS beamline 8.3.1 was evaluated by measuring the flux through a 10 μm tantalum pinhole as the pinhole was scanned through the beam at the sample position. These data match a Gaussian profile with full width at half-maximum (FWHM) of 120 μm × 108 μm (horizontal × vertical) with a root-mean-square residual that is 1.5% of the maximum flux through the 10 μm pinhole (data not shown). For this Gaussian profile the X-ray brightness at the edge of a 30 μm pinhole is not less than 6% lower than the brightness in the middle. The average brightness over the area of the pinhole is 98% of the peak brightness in the center of the beam. Since the pinhole was only 12 mm from the sample position and the maximum beam divergence was 3 mrad, the peak brightness of the uncollimated X-ray beam at the sample is negligibly different from the peak brightness of the beam at the pinhole. When using the 30 μm pinhole, the peak brightness of the 'dosing beam' was calculated to be the measured flux divided by the area of a 30 μm-diameter circle.

For the 100 μm pinhole, the brightness at the edge of the pinhole is 52% of the brightness in the middle and the average brightness is 77% of this peak brightness. The numerical integral of the decay experiment was performed over the beam profile (a 120 μm × 108 μm Gaussian 'chopped' at 50 μm radius). The result of this simulation (not shown) was that the half-reaction dose ($D_{\frac{1}{2}}$) observed using the 100 μm pinhole would be systematically 78% of the $D_{\frac{1}{2}}$ observed using the 30 μm pinhole (if one assumed that the beam brightness did not vary across the 30 μm pinhole). There is a small (<1%) secondary correction that depends on the magnitude of the decay rate itself, but this was not applied. In practice, this 78% correction was applied to experiments that used the 100 μm pinhole and the corrected decay rates were found to match those measured with the 30 μm pinhole. Nevertheless, whenever possible, comparisons of decay rates were performed between experiments that used the same pinhole size at the same beamline.

The 'burn' phase of these experiments used uncollimated beam to prevent sample drift from bringing 'fresh' sample in and out of the beam over time and introducing systematic errors. However, the dose was calculated for the cylindrical region of the sample that experienced the 'probe beam'. This assumption is valid provided that there was little or no energy transfer in the sample perpendicular to the beam axis on the length scale of the pinhole. For example, during the 'burn', photons fluoresced from Se atoms outside of the region probed by XANES could be re-absorbed by atoms inside the XANES-probed volume. This would add to the dose absorbed by the XANES-probed volume and it certainly does occur, so the dose calculation described above is a slight underestimate. However, the highest concentration of Se used in these experiments was 500 m*M*. At this concentration the total energy going into fluorescence from Se amounts to 32% of the total energy initially absorbed by the sample (about 2% of the incident beam). The self-absorption of the fluorescent photons is difficult to model exactly, but if all these photons were incident on the sample as a beam then only 2% of them would be absorbed. So the magnitude of the underestimate of dose due to fluorescence is most likely less than 1%.

In addition to the uncollimated 'dosing beam', some dose was delivered to the sample during the diffraction measurements as well as during the XANES sessions. The 'diffraction beam' was simply the 'dosing beam' with the same aperture as the XANES sessions. The sample was re-aligned with the pinhole just prior to each diffraction measurement, so the dose deposited by the 'diffraction beam' had a very similar profile to the dose deposited by the 'dosing beam' over the XANES-probed region of the sample. For this reason the diffraction exposure times were simply added to each 'burn'.

Unless noted otherwise, the total X-ray fluence (photons/area) experienced by the sample from the 'probe beam' (attenuation optimization and all XANES measurements) was less than 1% of the total fluence experienced by the sample in the entire run. Therefore, the dose deposited by the smaller beam profile and different photon energies explored by XANES was not significant. Nevertheless, the photons experienced by the sample during XANES were included in the dose calculations with the caveat that all photons were considered to have the same energy as the 'burn'.

2.8. Flux calibration

ALS beamlines 8.3.1 and 12.3.1 are equipped with PIN photodiodes for monitoring the beamline flux. The diode in each beamline is mounted on a pneumatic plunger that inserts the diode between the sample position and the beam stop. The diodes are 'in line' and experience the full flux of X-rays passing through the sample position less those photons

absorbed in the short air path and 40 μm of Al foil used to shield the diodes from visible light.

The built-in PIN photodiode at ALS beamline 8.3.1 (model S-100VL available from OSI Optoelectronics) is attached in unbiased photoconductive mode to a current amplifier (Stanford Research Instruments model SR570). This diode was calibrated against a NaI:Tl scintillator (Oxford Danfysik model CBY38NA01B) connected to a single-channel analyzer (Oxford Danfysik model CyberStar X1000). To avoid saturating the scintillator, the X-ray beam was attenuated by detuning the rocking curve of the monochromator, inserting metal filters and adjusting the beam divergence apertures until approximately 100000 counts s^{-1} were registering on the scintillator. The difference in diode current with the X-ray shutter open and closed was averaged for 10 s to measure the ~25 pA of current to a precision of 2%. The count rate was corrected for absorption in the 200 μm Be window in front of the scintillator, the small air gap between the scintillator and the sample position as well as for Poissonian undercounting by the 1 μs dead-time of the single-channel analyzer. It was found that a photon flux of 2.83×10^6 X-ray photons s^{-1} passing through the sample position at 12680 eV produce a 1 nA current from the diode. The calibration was repeated ten times and the standard deviation of the counts/amp sensitivity results was 5%. This calibration procedure was first performed in 2003 and again shortly after all the data presented here were collected. The measured sensitivity was the same. It is therefore unlikely that the X-ray beam damaged this diode over the course of these experiments.

The built-in PIN photodiode at ALS beamline 12.3.1 (model PIN-10DPI available from OSI Optoelectronics) is attached in unbiased photoconductive mode to a current amplifier (Stanford Research Instruments model SR570). The diode was calibrated against the diode in ALS 8.3.1 by comparison of the diode currents on both beamlines with a portable PIN diode (model S-25V available from OSI Optoelectronics). The response of all three diodes to 12680 eV photons was found to be within 5% of each other, so the calibration of 2.83×10^6 photons s^{-1} nA^{-1} was also used at 12.3.1.

Some PIN diodes have a high series impedance that causes them to become nonlinear at high currents, but the built-in diodes used in these experiments were found to be linear over the current ranges measured here. The linearity of each diode was verified by inserting and removing nine combinations of attenuator foils and comparing the diode current to the current produced in a He-filled ion chamber in the same beam. The diode currents were proportional to the ion chamber current and the current reading with multiple foils inserted was equal to the current expected by multiplying the transmittances of the individual foils, indicating good linearity.

2.9. Data processing and interpretation

Since a 'half-life' generally refers to the passage of time, and the decay of SeMet appears to depend much more on the delivered dose than on elapsed time, the term 'half-dose' ($D_{\frac{1}{2}}$) is used here to describe the robustness of SeMet in a sample. Here the $D_{\frac{1}{2}}$ of the SeMet side chain is defined as the dose required to destroy half of the SeMet in the sample, or, more practically, the dose required to reduce the height of the 'white line' halfway to the high-dose baseline. $D_{\frac{1}{2}}$ was measured by fitting a single exponential curve to the plot of the cross section at the peak against absorbed dose, and the dose at which the exponential function decays to 0.5 is assigned as $D_{\frac{1}{2}}$ for the SeMet in that sample (Fig. 2).

The term 'protection factor' is used to compare pairs of $D_{\frac{1}{2}}$ measurements. This quantity serves to measure how much a particular additive or other experimental parameter impacts the $D_{\frac{1}{2}}$ of SeMet. It is computed as the absolute difference in the $D_{\frac{1}{2}}$ measurements, divided by the smaller of the two $D_{\frac{1}{2}}$ values. For example, the $D_{\frac{1}{2}}$ of SeMet in the GCN4 crystal was 43 ± 2 MGy, and the $D_{\frac{1}{2}}$ of SeMet prepared in that crystal's cryoprotectant was 14.2 ± 0.6 MGy. Therefore the 'protection factor' of this crystal is 204 ± 20%. That is, the SeMet withstood ~200% more dose in the crystal than it did as a free amino acid under the same solution conditions. Fig. 3 illustrates the protection factor calculation for nitrate ions.

2.10. Sources of error

Apart from the random error associated with photon counts, there are other potential sources of error. Fluctuations in incident beam intensity can be controlled but never completely eliminated. For this reason, repeated measurements were made for the ten critical energies in each XANES session. The error of the cross-section measurement of each XANES session was estimated from the scatter in these repeated measurements and these errors were propagated

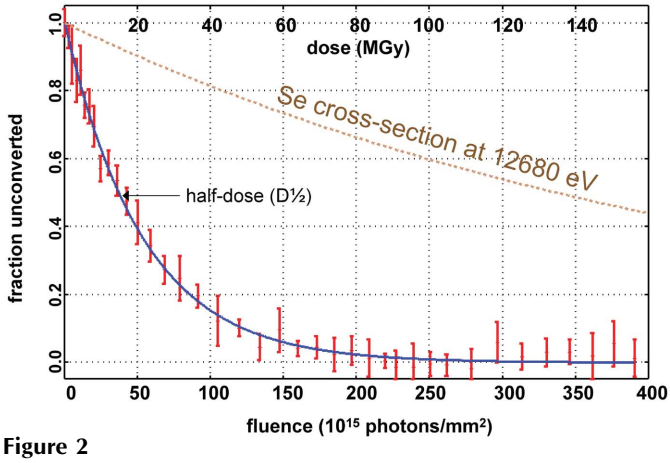

Figure 2
Normalized plot of the fraction of unconverted SeMet (red error bars) against the X-ray fluence experienced by the sample at 12680 eV (droplet 38 from Table 1). The dose absorbed by the sample is indicated on the top *x*-axis and the fluence delivered is on the bottom *x*-axis. The blue solid line is the best-fit exponential curve to the data. The dotted brown line represents the fraction of selenium atoms in the sample that have experienced one or more direct collisions with an X-ray photon (photoionization events). Here we use a photoionization cross section of 157 cm^2 g^{-1} for Se at 12680 eV (Hubbell, 1982). Clearly, the change in the XANES spectrum is too fast to be a direct result of primary photoionization of SeMet by X-ray photons. The breakdown of the Se—C bond must be the result of secondary or tertiary events.

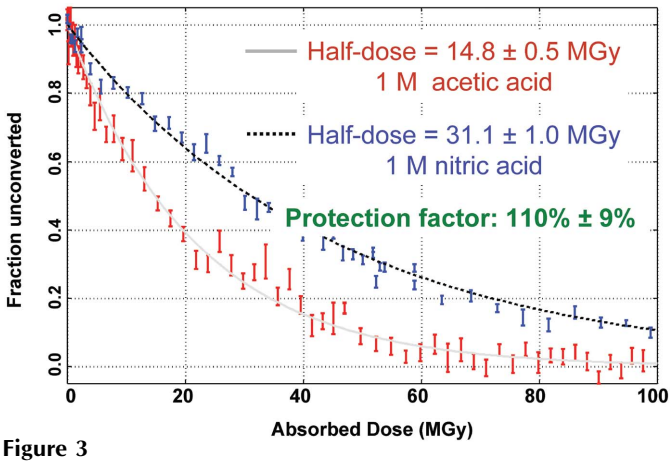

Figure 3
Protection factor of nitrate ions. The fractional progression of the damage suffered by a solution of 25 m*M* SeMet in 25% (*v*/*v*) glycerol with either 1 *M* acetic acid (red error bars) or 1 *M* nitric acid (blue error bars) and the best-fit exponential curves to those data (solid grey and dotted black lines, respectively). The dose at which half of the SeMet has been damaged is called the 'half-dose' ($D_{\frac{1}{2}}$) for that sample. The difference between the $D_{\frac{1}{2}}$ of the nitric and acetic acid solutions divided by the $D_{\frac{1}{2}}$ of the acetic acid sample is called the 'protection factor', and reflects the degree of the positive impact nitrate ions have on the $D_{\frac{1}{2}}$ of SeMet. Errors in the $D_{\frac{1}{2}}$ determinations are propagated to evaluate whether the protection factor is significant.

through to the curve-fitted $D_{\frac{1}{2}}$ value. Limited beam time did not permit more than one $D_{\frac{1}{2}}$ measurement for most of these sample types. Whenever possible the error in $D_{\frac{1}{2}}$ for a given sample type is given from the scatter in measurements from multiple samples. However, unless noted specifically, the error intervals assigned to $D_{\frac{1}{2}}$ values reported here is the error propagated from the data of a single decay run. These errors are given in Table 1.

The most important caveat for the data presented here is that the XANES spectrum of the damaged SeMet species is sloped at the 'white line' photon energy of the undamaged SeMet. This means that once a large fraction of the SeMet is damaged, a small drift in the incident photon energy will influence the apparent progression of the SeMet breakdown reaction. The slope at this point in the spectrum of damaged SeMet is 11 $cm^2\ g^{-1}$ per eV of drift. The peak height over the damaged baseline is 63 $cm^2\ g^{-1}$ so an error of 0.18 fractional conversions is introduced for a 0.5 eV drift. Since 0.5 eV is the limit of the peak lock, systematic errors as large as 18% are possible in the $D_{\frac{1}{2}}$ measurements presented here.

3. Results

3.1. Two-state decay reaction

Reference XANES spectra of undamaged SeMet and thoroughly damaged (500 MGy) SeMet were collected and compared with the XANES spectra obtained during the decay measurements. When normalized to the incident beam intensity, to within experimental error, all the XANES spectra taken from the samples in this work can be represented as a linear combination of the two reference spectra. This result is consistent with there being only two species present at any concentration during the decay reaction. There would appear to be no intermediate species with different XANES spectra from SeMet and the primary decay product, and if there are intermediates they must have a similar Se bonding environment to either the reactant or the product. The two-state hypothesis is further supported by the XANES session data. The $D_{\frac{1}{2}}$ results presented here reflect the peak height relative to the high- and low-energy baseline measurements, but the ratio of the counts at the peak and 'valley' energies also decayed with the same exponential $D_{\frac{1}{2}}$ (data not shown). Observing the same decay rate for different parts of the spectrum is evidence that the transformation from SeMet to its decay products is a two-state process.

3.2. Factors that did not affect the radiation damage rate of SeMet

Since the mechanism of SeMet breakdown with dose is not clear, it is instructive to first describe the experimental factors that were observed not to have a significant influence on the $D_{\frac{1}{2}}$ of SeMet. This is important for selecting pairs of experiments to serve as controlled pairs for an experimental parameter of interest. Note that the error assigned to these measurements was generally of the order of 20%. Some of the factors described as having 'no effect' here may indeed have an effect that is of the order of 20% that was not detected by the analysis below.

3.2.1. Sample dimensions. The thickness, total volume and overall shape of the solution droplets is difficult to reproduce precisely in nylon loops, but repeated measurements using the same solution in different loops with different droplet thicknesses was found not to change the $D_{\frac{1}{2}}$ of SeMet within experimental error (for example, see droplets 73 and 78 in Table 1). These droplets were samples of the same solution, but droplet 73 was oriented with the loop 'edge-on' to the X-ray beam to maximize the path the X-ray beam took through the sample (328 µm). Droplet 78 and all samples other than droplet 73 were oriented 'face-on' with the beam passing normal to the plane of the loop. The protection factor of loop orientation between droplet 73 and droplet 78 is 12 ± 5%. Since these two samples were otherwise identical in chemical composition and physical state, this difference represents the maximum systematic error introduced by sample dimensions.

3.2.2. Time. Do SeMet side chains continue to break after the beam is turned off? The individual fluorescence measurements within each XANES session were time-stamped and these 'raw' data from the 25 m*M* SeMet in 15% (*v*/*v*) MPD and 5% (*w*/*v*) PEG8K (droplet 34 in Table 1) are plotted in Fig. 4. One can see that, although the trend of the decay curve was clear, the individual observations were noisy. Therefore, the temporal resolution of this study was not better than 10 min (the duration of a XANES session).

The experiment plotted in Fig. 4 was interrupted at the 5 h mark and resumed 5 h later. The fraction of unconverted SeMet did not change noticeably during this 'dark' period during which the sample remained under liquid nitrogen.

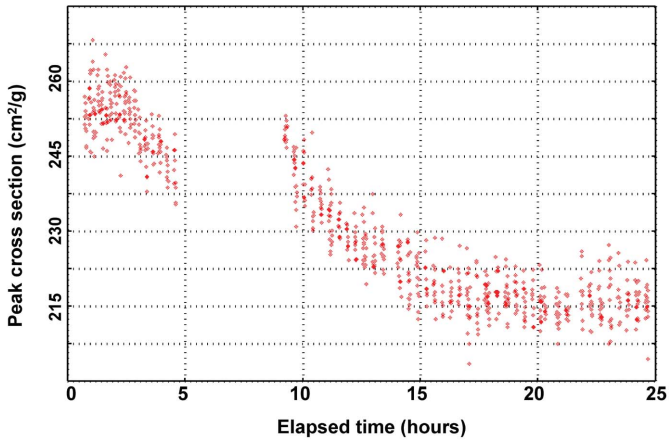

Figure 4
This interrupted experiment demonstrates a lack of 'dark progression' of SeMet breakdown. Individual measurements of the peak 'white line' absorbance cross section are plotted against the time elapsed since the beginning of the experiment. The depicted run was interrupted after 5 h and the sample was returned to liquid nitrogen. After a 5 h delay, the sample was mounted, re-centered, and the rest of the decay curve was measured. There is no apparent change in the height of the white line across the 5 h during which the experiment was interrupted. When these data are plotted against the absorbed dose instead of time, they follow an exponential decay (Fig. 2).

Other partially dosed samples were stored for much longer periods (up to a week) with no apparent change in the XANES spectrum. Whatever the mechanism of SeMet disruption, it apparently went to completion in less than 10 min after the beam was removed and damage did not continue hours and days after the X-rays had stopped. This fact proved to be useful for measuring SeMet damage rates, because the experiment could utilize small blocks of beam time. This is also valuable information for scheduling protein crystal data collection, since it can be expected that a partially damaged SeMet-containing crystal can be safely removed and replaced at a later date for further data collection.

3.2.3. Dose rate. A dose-rate dependence was recently reported for the decay of SeMet sites (Leiros *et al.*, 2006). Leiros *et al.* examined SeMet breakdown at dose rates ranging from 47.5 to 475 kGy s^{-1}. The dose rate here was usually allowed to vary with the ALS ring current and ranged from 5 to 25 kGy s^{-1} (see Table 1) and no conscious attempt was made to measure a dose rate dependence. However, its existence would have introduced a systematic error between $D_{\frac{1}{2}}$ values obtained from samples that experienced different dose rates during the critical first half-life of the decay curve. To test for this, two experiments were selected that had been performed on the same substance, but with the largest difference in mean dose rate during the first half-life of the run: droplet 102 (6.0 kGy s^{-1} over the first half-life) and droplet 90 (8.5 kGy s^{-1} over the first half-life). The samples were 31 m*M* SeMet in 0.6 *M* NaOH and 25% glycerol in an amorphous state, and the protection factor between these two experiments is 0 ± 3%. This indicates that any difference in apparent $D_{\frac{1}{2}}$ due to the difference in dose rate is smaller than the errors introduced from other sources. The average $D_{\frac{1}{2}}$ for the nine samples of this substance measured at 8.3.1 with no dose rate control (droplets 74, 85, 88, 89, 90, 101, 102, 103 and 104) was 12.6 ± 0.7 MGy. Eight other samples of the same substance (107, 113, 114, 115, 120, 121, 125 and 128) were measured at 8.3.1 with the dose rate limited to a constant 4.5 MGy s^{-1} by actively adjusting the divergence slits in the beamline to compensate for the ALS ring current. The average $D_{\frac{1}{2}}$ from these eight dose-rate-controlled runs was 12.2 ± 0.5 MGy. The scatter in the $D_{\frac{1}{2}}$ values is smaller, but this is not a statistically significant difference. It was concluded from these observations that no dose rate dependence was detectable in this work.

3.2.4. Selenium concentration. Since the two protein crystal types studied here had different total Se concentrations (92.3 m*M* for GCN4 and 32.6 m*M* for NE1) than many of the solution SeMet samples (25 m*M*), a series of SeMet concentrations in solution were needed as a frame of reference to answer the question of whether the concentration of SeMet affects the lifetime.

The $D_{\frac{1}{2}}$ of SeMet for a range of SeMet concentrations was measured in 0.6 *M* NaOH and 25% glycerol in an amorphous state (droplets 47, 49, 55, 59, 88, 89, 90, 102, 103 and 104). The high pH was chosen because 500 m*M* SeMet is not soluble at neutral pH and also to eliminate the putative electron-scavenging effect of protons and expedite the experiments. It was found that concentrations of SeMet between 16 m*M* and 500 m*M* all resulted in a common $D_{\frac{1}{2}}$: 12.6 ± 0.3 MGy on average. Individual $D_{\frac{1}{2}}$ values are given in Table 1. This invariance of $D_{\frac{1}{2}}$ with concentration suggests that samples with different SeMet concentrations can be considered comparable. For example, comparing the $D_{\frac{1}{2}}$ of a crystal containing 92 m*M* SeMet (such as droplet 32) with the $D_{\frac{1}{2}}$ from solution of 31 m*M* SeMet in the same cryoprotectant (such as droplet 34) is an appropriate control for the influence of the protein crystal because a solution of 92 m*M* SeMet is expected to have the same $D_{\frac{1}{2}}$ as 31 m*M* SeMet. The concentration independence of $D_{\frac{1}{2}}$ also implies that any errors in the concentration of SeMet due to evaporation of sample drops in the few seconds prior to flash-cooling, pipette calibration errors or electrostriction effects from mixing SeMet stocks with concentrated additive solutions did not impact the measured $D_{\frac{1}{2}}$.

3.2.5. Incident photon energy. In general, the more dose a sample absorbs, the more damaged it becomes. Unfortunately, MAD and SAD experiments require photon energies that optimize the absorbance of the sample. One would expect that damage to the heavy-atom sites (which have the highest cross sections) would be at its worst under these conditions. Is this really the case?

The choice of incident photon energy did not have a significant impact on the $D_{\frac{1}{2}}$ of SeMet decay. The $D_{\frac{1}{2}}$ value was measured using incident photons of either 12680 eV or 12540 eV in energy. The solution samples were all 31 m*M* SeMet in 0.6 *M* NaOH and 25% glycerol in an amorphous state. A $D_{\frac{1}{2}}$ value of 13.3 ± 0.3 MGy was measured using 12540 eV photons (droplet 128). The closest-in-time measurement of this same material that used 12680 eV photons to deliver the dose and had a similar maximum dose was droplet 125 which gave $D_{\frac{1}{2}}$ = 12.5 ± 0.2 MGy. The

protection factor is 6.1 ± 3% for low-energy over high-energy illumination. The average $D_{\frac{1}{2}}$ value of the 19 samples of this material using 12680 eV to deliver the dose was 12.3 ± 0.9 MGy. The protection factor using this average $D_{\frac{1}{2}}$ of high-energy photons is 8.5 ± 8%. There does not appear to be a significant difference, but it should be noted that these measurements were normalized to absorbed dose. A higher fluence (photons/area) of 12540 eV photons is required to deposit 1 MGy into this sample than is required of 12680 eV photons. In practice, more diffraction data can be collected per unit of dose at 12540 eV than at 12680 eV. However, this difference for 31 m*M* SeMet is only 3%. The choice of photon energy did not appear to significantly impact the radiation damage rate of SeMet in this study.

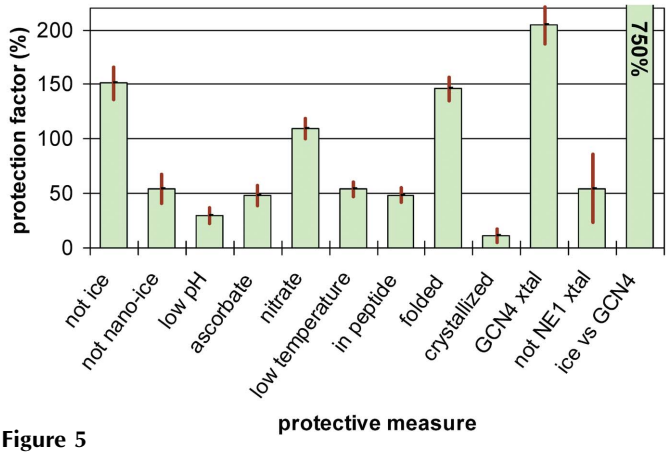

Figure 5
Some experimental parameters protect SeMet from radiation damage. The 'protection factor' is the fractional increase in the 'half-dose' ($D_{\frac{1}{2}}$) of SeMet when the indicated 'protective measure' is used. The $D_{\frac{1}{2}}$ is the X-ray dose that will damage half of the SeMet in the sample. The 'not ice' column shows the protection factor of rapidly cooling a solution of SeMet to form an amorphous glassy solid as opposed to cooling it slowly to form ice Ih (droplet 110 in Table 1). The 'not nano-ice' column shows the protection factor of the same amorphous condition over the same solution cooled slightly slower to form the nano-crystalline solid discussed in the text (droplet 130). 'Low pH' is the protection factor of preparing the amorphous sample with 1 *M* acetic acid added to the solution over adding 0.6 *M* NaOH (droplets 39 and 52). 'Ascorbate' is the protection factor of using 1 *M* ascorbic acid instead of acetic acid (droplets 20 and 21). 'Nitrate' is the protection factor of using 1 *M* nitric acid instead of acetic acid (droplets 25 and 21). 'Low temperature' is the protection factor of running the experiment at 93 K instead of 140 K in 0.6 *M* NaOH (droplets 86 and 88). All other experiments in this figure were run at 93 K. See Fig. 6 for details. 'In peptide' is the protection factor of unfolded GCN4-N16A-p1 peptide at 20 m*M* (80 g L^{-1}) boiled in 9.5 *M* urea over free SeMet at 25 m*M* also boiled in 9.5 *M* urea with 80 g L^{-1} insulin. 'Folded' is the protection factor of folded GCN4-N16A-p1 peptide in solution (no urea) over the same concentration of unfolded peptide (boiled in 9.5 *M* urea). 'Crystallized' is the protection factor for GCN4-N16A-p1 peptide crystals over the folded peptide in solution. 'GCN4 xtal' is the protection factor of a crystal of the GCN4-N16A-p1 peptide over free SeMet in the crystal cryoprotectant. This combines the previous three protective measures. 'Not NE1 xtal' is the protection factor of a crystal of free SeMet in solution over the SeMet side chains in the E1 domain of NEDD8, but note that not all crystals are protective. 'Ice vs GCN4' is the protection factor of the largest observed $D_{\frac{1}{2}}$ (43.2 MGy) over the smallest observed $D_{\frac{1}{2}}$ (5 MGy). This final protection factor is 750% and dwarfs all the others, so it is indicated by a number over the graph. Although individual protection factors are small enough to be difficult to measure, the effects were generally additive and the range of observed $D_{\frac{1}{2}}$ values for SeMet does vary widely.

3.3. Factors affecting the radiation damage rate of SeMet

The factors found to significantly influence radiation damage rates to SeMet are summarized in Fig. 5. The temperature, the structure of the protein, the crystalline phase of the cryoprotectant and the introduction of additives were all found to have a significant impact.

3.3.1. Temperature. Would going to even lower temperatures cause SeMet to last longer? How much faster will it decay at higher temperatures? To answer these questions, the $D_{\frac{1}{2}}$ of amorphous samples of 31 m*M* SeMet in 0.6 *M* NaOH and 25% glycerol (droplets 74, 86, 87, 88, 89, 90, 92, 94, 100, 102 and 106) was measured at different temperatures (Fig. 6). These measurements indicate a protection factor of about 0.6% K^{-1} between 93 K and 130 K, and about 2% K^{-1} between 130 K and 155 K.

This temperature dependence can also be evaluated in terms of the Arrhenius equation,

$$k = A \exp\left[-E_{\rm act}/(RT)\right],$$

where k is the reaction rate constant [equal to $\ln(2)/D_{\frac{1}{2}}$/dose-rate], $E_{\rm act}$ is the activation energy of the damage reaction, T is the absolute temperature, R is the ideal gas constant and A is the 'frequency factor', which is generally related to the fraction of collisions between reactants that have the 'correct orientation' to react. The values of $E_{\rm act}$ and A are obtained from the slope and intercept, respectively, of a plot of ln[ln(2)/$D_{\frac{1}{2}}$/dose-rate] against $1/T$. The low-temperature (at or below 130 K) and high-temperature (at or above 130 K) data in Fig. 6 correspond to Arrhenius activation energies ($E_{\rm act}$) of 0.5 and 4.4 kJ mol^{-1}, respectively, and 'frequency factor' (A) values of 5×10^{-4} and 2×10^{-2}. The 'frequency factor' is 36-fold smaller below 130 K. That is, the shallow temperature

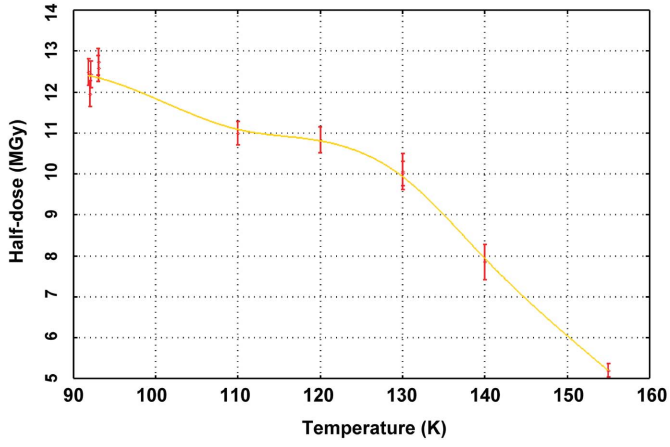

Figure 6
Temperature dependence of the $D_{\frac{1}{2}}$ of 31 m*M* SeMet in 0.6 *M* NaOH and 25% (*v*/*v*) glycerol. $D_{\frac{1}{2}}$ values for samples of this solution were measured with the sample cooler set for different temperatures (error bars). Lower temperatures continued to increase the $D_{\frac{1}{2}}$ of SeMet down to ∼92 K which was the lowest temperature obtainable with this equipment. The solid line is a smooth curve (to guide the eye). There is a clear transition in the slope of the temperature dependence of the $D_{\frac{1}{2}}$ around 130 K which may correspond to the glass transition of pure water near this same temperature, allowing new factors to come into play above 130 K.

dependence of the radiation-damage reaction suggests a process with a low activation barrier, and the 'kink' in the curve suggests 36-fold less productive collisions with the damaging species below 130 K. Since the concentration of the damaging species is not known, this interpretation cannot distinguish between each collision having a lower probability of reaction or fewer total collisions.

Since the glass transition temperature of pure water is at 136 K, it is plausible that a similar drop in viscosity occurs in vitrified 25% glycerol at a similar temperature. The increased temperature dependence of the SeMet $D_{\frac{1}{2}}$ above 130 K could then be explained by the increased mobility of the damaging species or the introduction of one or more new reactive species that are trapped at lower temperatures. XANES data did not support the addition of a new decay product at higher temperature. The final XANES spectrum at 155 K is indistinguishable to within experimental error from the final XANES spectrum from samples dosed at any other temperature (data not shown). This temperature dependence is consistent with a rate-limiting energy-transport mechanism at high temperature (with $E_{\rm act} \simeq 4$ kJ mol^{-1}) that ceases to be available below 130 K. A second energy-transport mechanism (with $E_{\rm act} = 0.5$ kJ mol^{-1}) becomes significant below the glass transition. That is, the rate-limiting barrier of the second mechanism is lower, but the 'frequency of collisions' is also lower.

Note that the higher-temperature samples are listed in Table 1 as having a non-zero fraction of nano-ice. However, all of these samples were 100% amorphous when mounted and began slowly converting into nano-ice when the stream temperature was raised. At 155 K the sample (droplet 100) took 7 h to convert from 25% to 77% nano-ice; the fractions listed in Table 1 represent the average nano-ice fraction over the experiment. This conversion was not caused by the X-ray beam, since a control droplet (not shown) mounted in an amorphous state and left at 155 K overnight converted from 0 to 40% nano-ice in 8 h.

3.3.2. Solvent structure. The method of cryoprotection has a significant impact on how fast SeMet decays. Specifically, the crystalline phase of the flash-cooled cryoprotectant was found to have a dramatic effect on SeMet lifetime. Admittedly, the formation of crystalline ice in a protein crystal during flash-cooling is expected to destroy the diffraction because formation of ice Ih expands the material in the solvent channels, disrupting the lattice (Weik *et al.*, 2001, 2005). Since ice destroys diffraction, it might be assumed that the radiation damage rate in icy phases is not relevant to protein crystal data collection. However, the background of many protein crystal diffraction patterns taken at the ALS suggests a semi-crystalline state of the flash-cooled cryoprotectant that was apparently dense enough to still be compatible with the protein crystal lattice. For example, the background from one of the GCN4 crystals (droplet 32) corresponds to this semi-crystalline state, as does the cryoprotectant used for these crystals flash-cooled on its own.

This semi-crystalline phase is transparent at optical wavelengths and most likely made up of very small crystals of cubic ice. The diffraction pattern consists of rings at the *d*-spacing of the (111), (022) and (131) reflections from cubic ice Ic (3.67, 2.247 and 1.917 Å, respectively). However, these rings are not sharp. The 3.67 Å ring width averaged $\Delta\sin(\theta)/\lambda = 8.77 \pm 1.1$ mrad Å^{-1} FWHM. The rings from fully crystalline ice would have been sharper (the divergence of the X-ray beam: 2 mrad). If the width of the primary ring is interpreted as the line broadening of a Bragg peak from a small crystal (Woolfson, 1970) then the crystallites are of the order of 5–6 nm in size (approximately ten unit cells wide). For this reason, this substance will be referred to as nano-crystalline cubic ice or 'nano-ice'. The diffraction rings from nano-ice are close to the *d*-spacing of the first two rings of the amorphous solid (at 3.57 and 2.08 Å), which are also broader than the nano-ice rings. Thus, the rings from nano-ice are easily masked by or mistaken for the rings from amorphous solvent. Indeed, if the widths of the rings in the amorphous solid are interpreted as a crystal size, then the equivalent crystallite dimension is 1.25 nm, which is exactly twice the cell dimension of cubic ice Ih (6.358 Å). Many diffraction patterns observed here had characteristics of both nano-ice and amorphous solid and in these cases the observed diffraction pattern was fitted to a linear combination of the diffraction patterns of both. The '%nano-ice' values obtained in this way are reported in Table 1. The results are consistent with nano-ice and amorphous phases co-existing in the same sample; however, it is also possible that these apparent mixtures simply represent a continuum of crystallite sizes between nano-ice (ten unit cells of ice Ic) and an amorphous solid (two unit cells).

The average $D_{\frac{1}{2}}$ from two samples (droplets 130 and 131) of 31 m*M* SeMet in 0.6 *M* NaOH and 25% glycerol that cooled to the nanocrystalline state is 8.0 ± 0.5 MGy. The average $D_{\frac{1}{2}}$ of 19 samples of the same substance cooled into an amorphous solid state was 12.3 ± 0.9 MGy. Cooling to a completely amorphous state represents a protection factor of $54 \pm 10\%$.

Another sample of the same substance (droplet 110) was warmed and slowly cooled to convert the water content into crystalline ice. The diffraction pattern of this sample exhibited characteristic sharp ice rings, indicating ice Ih, and the $D_{\frac{1}{2}}$ measured from this sample was 5.0 ± 0.2 MGy. The average $D_{\frac{1}{2}}$ from amorphous samples of the same substance on the same beamline using the same pinhole (droplets 73, 97, 99, 108 and 111) was 12.8 ± 0.7 MGy. This represents a dramatic protection factor of $151 \pm 10\%$ for an amorphous vitrified solid over crystalline ice.

The impact of nanocrystalline cryoprotectant did extend to protein crystals, but it had the opposite effect. One GCN4 crystal (droplet 31) exhibited a diffraction background consistent with an amorphous solid and the other (droplet 32) was nano-ice. The protection factor between these samples was $36 \pm 7\%$ for nano-ice over the amorphous solid. Although this is a single result, the protection factor is statistically significant. These two crystals were dosed with different photon energies, but the choice of photon energy was demonstrated to have no impact on the decay rate of other samples (such as droplets 125 and 128). It is possible that the mechanism of damage acceleration by nano-ice interacts in a

non-linear way with the mechanism of damage protection by protein structure.

3.3.3. Protein structure. If the microscopic structure of the cryoprotectant affects the $D_{\frac{1}{2}}$ of SeMet, what about protein structure? In some cases protection by protein tertiary structure was dramatic, but it was not a general property. A crystal of the NEDD8 E1 domain yielded a SeMet $D_{\frac{1}{2}}$ of 11 ± 3 MGy (droplet 29), which was less than SeMet in free solution. That is, the protection factor afforded by dissolving SeMet in free solution as opposed to placing it in the NE1 crystal was $55 \pm 30\%$ (droplet 38 over 29). This may not have been statistically significant, but it is clear that the lifetime of the SeMet side chain in the NE1 crystals was not longer than that in the free amino acid.

On the other hand, crystals of the GCN4-N16A-p1 peptide afforded a great deal of protection to the SeMet residues of this peptide. The electron density of all three Se sites in trigonal crystals of GCN4-N16A-p1 showed no evidence of damage with increasing X-ray dose (data not shown). The diffraction faded away first, decaying from 1.8 Å to 9 Å after ~30 MGy. By the XANES probe, however, one of these crystals (droplet 32) yielded the highest $D_{\frac{1}{2}}$ measured in this work: 43 ± 2 MGy. This is 3.5-fold higher than the $D_{\frac{1}{2}}$ of free SeMet in glycerol (droplet 38; 17 ± 0.5 MGy). The protection factor is $250 \pm 30\%$. What property of these crystals leads to such a dramatic protection factor?

The $D_{\frac{1}{2}}$ of free SeMet dissolved in the cryoprotectant used for the GCN4-N16A-p1 crystals (droplet 34) was 14 ± 0.6 MGy. This was lower than the $D_{\frac{1}{2}}$ of free SeMet dissolved in glycerol (droplet 38), which was 17 ± 0.5 MGy. Indeed the crystal cryoprotectant cooled as partial nano-ice and not as an amorphous solid. The difference in crystalline phase was likely to have been the source of the difference in $D_{\frac{1}{2}}$ between droplet 34 and droplet 38. The protection afforded by the GCN4 crystals (droplets 31 and 32 over droplet 34) must have come from the peptide. The $D_{\frac{1}{2}}$ of SeMet in the peptide after boiling in 9.5 *M* urea was 16 ± 0.6 MGy (droplet 66). This was 50% higher than the $D_{\frac{1}{2}}$ of free SeMet after boiling in 9.5 *M* urea, which was 10.6 ± 0.3 MGy (droplet 68). Bovine insulin was added to droplet 68 as a control so that 100 g L^{-1} of protein was present in both droplets. To control for the presence of urea, the GCN4 peptide was prepared by combining the stock with a saturated solution of urea at 40% (*v*/*v*) but this was not boiled prior to mounting (droplet 63). The folded peptide was also prepared in the absence of urea (droplets 43 and 53) and the average $D_{\frac{1}{2}}$ from these two droplets of folded peptide was 34.7 ± 4 MGy, so the protection factor for folding the peptide was $120 \pm 30\%$ (droplets 43 and 53 over 66). The insignificant protection factor of the folded peptide over the non-boiled 40% saturated urea preparation ($14 \pm 20\%$) demonstrated that the peptide was still folded under these conditions and suggested that the presence of urea in the solution was not directly influencing the $D_{\frac{1}{2}}$. All urea-containing samples were amorphous.

Crystallizing the peptide afforded no apparent protection to the SeMet residues. The $D_{\frac{1}{2}}$ measured from the crystallized peptide (droplet 32) was only $25\% \pm 10\%$ higher than the $D_{\frac{1}{2}}$ for the folded peptide in solution (droplets 43 and 53). This may not be a statistically significant difference. In summary, incorporation of SeMet into the covalent structure of this peptide afforded it some protection (50%), but the SeMet lifetime is more than doubled by folding the peptide. The protection factor of both incorporating SeMet into the peptide and folding it was $226 \pm 40\%$ (droplets 43 and 53 over 68). Incorporation of SeMet into the structure of this peptide had one of the most significant impacts on the decay rate of the SeMet side chain that was observed in these studies.

3.3.4. Stability in acids. Ascorbate ions have been shown to have a protective influence on disulphide bond breakage (Murray & Garman, 2002). Are there other additives that could enhance the lifetime of SeMet? Low pH, especially the addition of ascorbic acid or nitric acid, had a significant positive impact on the $D_{\frac{1}{2}}$ of SeMet. The protection factor of 1 *M* acetic acid over 0.6 *M* NaOH was $30 \pm 7\%$ (droplet 39 over 52). Smaller changes in pH were not tested, but the acetic acid/NaOH comparison covered the range of pH that most protein crystals will tolerate. Ascorbic and nitric acids (droplets 20 and 25, respectively) protected SeMet significantly more than acetic acid (droplet 21) with protection factors of $48 \pm 9\%$ and $110 \pm 9\%$, respectively. Tests of ascorbate and nitrate ion at neutral pH were not performed, but the mechanism of protection must have been more than just lowering the pH.

An important caveat for these results is that the crystalline nature of the cryoprotectant of these samples was not known (see Table 1) as diffraction data were not taken from these early samples. It is therefore possible that droplets 20, 21 and 25 had some nano-ice content that influenced the $D_{\frac{1}{2}}$. The diffraction pattern from a second acetic acid sample (droplet 39) did confirm a glassy state and the observed $D_{\frac{1}{2}}$ was slightly higher than droplet 21 (protection factor $13 \pm 6\%$). Although nano-ice was generally observed to lower the $D_{\frac{1}{2}}$, the $D_{\frac{1}{2}}$ values for ascorbate and nitrate were all larger than the $D_{\frac{1}{2}}$ of droplet 39, which was amorphous. Thus the protective nature of ascorbate and nitrate is qualitatively clear, but not quantitatively clear due to the uncertain physical state of the samples. The most relevant control sample for ascorbate and nitrate is therefore the one assayed closest to them in time, which is droplet 21.

4. Discussion

4.1. Proposed damage mechanism

The specific destruction of selenomethionine (SeMet) seen in protein crystallography experiments is most likely not to be due to direct interaction with X-ray photons. In all cases the changes in the XANES spectrum of Se atoms reached the half-reaction point significantly before half of the Se atoms in the sample had experienced a direct photon hit (Fig. 2). A dose of 170 MGy would have been delivered to a typical sample by the fluence of photons required to photoionize half the Se atoms, but the longest SeMet $D_{\frac{1}{2}}$ observed was 43.2 MGy, seen in crystals of the GCN4-N16A-p1 peptide, which is 8.2-fold

longer than the shortest $D_{\frac{1}{2}}$ observed (5.0 MGy for the icy droplet 110). Clearly the same number of X-rays does not do the same amount of damage to SeMet in different samples. Also, the addition of acetic acid, ascorbic acid or nitric acid has a significant positive impact on the $D_{\frac{1}{2}}$ of SeMet in free solution (roughly 30%, 50% and 110%, respectively). The positive impact of additives suggests that a mobile species must be responsible for the damage, although 'mobile' does not necessarily imply mass transport. There are many ways that energy can move through condensed matter without moving atoms, and the phenomenon of electricity is a familiar example.

The energy to break the Se—C bonds must have been initially absorbed in other parts of the sample and then transferred to SeMet. What fraction of the total deposited energy was transferred? The enthalpy of a Se—C bond was estimated as 590 kJ mol^{-1} (Kerr, 2000). Thus a dose of 18 kGy (18 kJ kg^{-1}) would be expected to be required to break half of the C—Se bonds in a solution of 31 m*M* SeMet, but this is 670-fold less than the observed $D_{\frac{1}{2}}$ of 12.3 MGy. The solution of 500 m*M* SeMet was also half-damaged by 12.3 MGy, but only 1/40th of that energy was required to break the bonds. The rest of the energy must have gone somewhere else. There are undoubtedly many possible relaxation pathways for the excited states generated by the immediate consequences of the absorbed photons. What can be inferred from the reaction kinetics?

The temperature dependence of $D_{\frac{1}{2}}$ suggested a very low Arrhenius activation barrier of 0.5 kJ mol^{-1} at temperatures below 130 K. This implies that the damage reaction is practically diffusion limited, which would make the damaging species the rate-limiting reactant. It is introduced in direct proportion to dose and it disappears quickly once the beam is removed. The invariance of the $D_{\frac{1}{2}}$ of SeMet for SeMet concentrations between 16 m*M* and 500 m*M* implies that the damage reaction is first-order with respect to SeMet concentration, but the existence of a dose-rate dependence of damage rate (Leiros *et al.*, 2006) suggests that the damage reaction has non-zero order with respect to the damaging species. As the dose rate increases, the rate of introduction of the damaging species is expected to increase proportionally but the recombination reaction-rate constants will be fixed. At a low dose rate the steady-state concentration of the damaging species will always be small and the reaction with SeMet will compete with all the other relaxation mechanisms. The damage reaction rate will therefore depend only on the concentration of SeMet and not on the dose rate. However, at some high dose rate, the rate of introduction of the damaging species will become comparable with the relaxation rates and the steady-state concentration of the damaging species will rise. These kinetic data are therefore consistent with a simple 'bimolecular collision' between SeMet and the damaging species as the mechanism for the radiation damage reaction.

What might be the nature of the damaging species? Since the medium of interest is a solid (no translational degrees of freedom) the possibilities for the identity of the mobile species are limited. The diffusion of molecular or even atomic radical species is an unlikely damage mechanism since the diffusion rate of any molecular species would be very slow in amorphous water at 95 K. The perfusion of hydrogen gas through a 26-molecule thick layer of amorphous solid water has been observed to take several minutes at 100 K (Petrik & Kimmel, 2004). However, absolutely no progression of the SeMet breakdown reaction is seen after the X-ray beam is turned off for several hours, and a slowly diffusing species would be expected to do some damage in that time. The protective impact of low pH points to mobile electrons, since unbound electrons tend to react with protons to form hydrogen atoms (Box, 1977). Hydrogen atoms can also inflict damage, but they should be much less mobile species than electrons since proton transfer is not as fast as electron transfer. Again the analogy with semiconductors is illuminating: electrons are much more mobile than 'holes' in silicon.

The influence of the crystalline state of the solvent on the $D_{\frac{1}{2}}$ of SeMet side chains can also be explained by a charged excitation transfer (mobile electron) damage mechanism. The amorphous, nano-crystalline and polycrystalline states of water had progressively enhancing impact on the radiation damage rate. Silicon also has amorphous, nano-crystalline and polycrystalline forms in addition to the well known single-crystal state. In general, the conductivity of electrons through these forms of silicon increases with the crystallite size. If the damaging species is analogous with the conduction-band electron in silicon, then it would be expected to more efficiently migrate through a more crystalline material. This would increase the likelihood of a mobile electron reacting with SeMet before it recombines with a hole. The frequency of recombination of electron–hole pairs in silicon also decreases with increasing crystallite size, and amorphous silicon has the highest recombination rate of all. By analogy, the purely amorphous form of water is expected to have a high recombination frequency in the bulk, so the damaging species is more likely to recombine than react with SeMet.

This model of the influence of sample microstructure on radiation damage can be extended to explain the influence of protein structure. Protein molecules, like any other solute, are surrounded by an electric field, and this electric field will often 'focus' on the active site of an enzyme (Honig & Nicholls, 1995). Computer simulations have suggested that the action of solvated electrons on DNA is strongly influenced by the electric field around the molecule (Soirat *et al.*, 1997; Milligan & Ward, 1994). In the solid state, mobile electrons can be expected to follow these microscopic field lines, jumping from water molecule to water molecule until they can give up their energy by reacting with something else. The physical process is analogous to the flow of excited states (electrons and holes) through amorphous silicon, except that the electric fields in a protein crystal are on a much smaller scale. This mechanism would explain why active-site residues seem to be particularly sensitive to radiation damage.

It has certainly also been observed by others (Burmeister, 2000; Leiros *et al.*, 2001; Weik *et al.*, 2001; Nukaga *et al.*, 2003; Fuhrmann *et al.*, 2004; Carugo & Carugo, 2005; Dubnovitsky *et al.*, 2005; Roberts *et al.*, 2005; Yano *et al.*, 2005) that the

position of a side chain in a structure has a significant positive or negative impact on sensitivity to radiation. Early observations suggested that solvent accessibility is correlated to the sensitivity of side chains to radiation (Ravelli & McSweeney, 2000; Weik *et al.*, 2000, 2002), but as more and more observations have been made this apparent correlation has become less clear (Carugo & Carugo, 2005; Fioravanti *et al.*, 2007). Long-lived sites with high solvent accessibility have been observed, and rapidly damaged side chains have been observed in protein cores. Active sites seem especially prone to radiation damage. It would appear that tertiary structure must influence the 'flow' of the species responsible for side-chain damage on the microscopic level and that the damaging species is not excluded from the core of the protein. The simplest explanation for these observations is a charged mobile excitation in the medium.

If the damaging species is a charged mobile excitation, then the apparent paradox of nanocrystalline ice enhancing the radiation damage rate in most cases but diminishing it in another (the GCN4 protein crystal) can be resolved. Since the folded GCN4 peptide structure has a protective influence on SeMet, the structure must generate an electric field that causes mobile electrons to avoid the SeMet site, possibly by directing them to a site where recombination is likely to occur. The covalent structure of the polypeptide backbone itself might be such a place (Pogocki *et al.*, 2001; Rauk *et al.*, 2000). This electric field is perhaps generated by the helix dipoles of the coiled coil. If the conductivity of the medium is enhanced by crystallinity, then the effect of this electric field would be enhanced. In this way the property of nanocrystalline ice (increased electronic conductivity) would play a protective role in the GCN4 crystals by enhancing the existing protective mechanism.

4.2. Advice for data collection

Since the lifetime of a SeMet site will most likely depend largely on the folded structure of the protein, the prospect of predicting SeMet lifetimes before the structure is solved appears to be bleak. However, protein structure is not the only determining factor in SeMet lifetime. Rapid flash-cooling to achieve a purely amorphous state is expected to have a significant positive impact. On the other hand, the only crystal type examined in both amorphous and nanocrystalline cryoprotectant is a counter example (droplet 32 *versus* 31). As with many parameters in protein crystallography, the impact of the phase state of the cryoprotectant may depend on the crystal in hand. Nevertheless, it is useful to know that the nano-ice or amorphous condition of the cryoprotectant can have a large impact on the radiation-damage rate.

Adding ascorbate has already been shown to extend the lifetime of disulphide bonds (Murray & Garman, 2002), and the evidence presented here suggests that ascorbate will protect SeMet as well. Nitrate ions appear to have a higher protective effect than ascorbate. Nitrate has yet to be tested near neutral pH, but its traditional use in ESR studies suggests that replacing any anions in a crystal with nitrate would be generally advisable.

Adjusting the pH of the sample to as low a value as possible is advisable. Every acid tried in these experiments extended the lifetime of SeMet. Care should also be taken with temperature-sensitive buffers such as tris or glycine, since the effective pH of these buffers can become quite high at cryogenic temperatures (Douzou, 1977).

The temperature of the sample is important, since higher temperatures do lead to more damage per unit dose, as described elsewhere (Weik *et al.*, 2001). In this study the same SeMet sample lasted 54% longer at 93 K than it did at 140 K. It does not appear that the temperature dependence of SeMet damage has 'leveled off' at the lowest temperatures tested, so it is expected that temperatures lower than 93 K will make SeMet last even longer. There is a much steeper dependence of the damage rate on temperature above 140 K, indicating that temperatures this high should be avoided if preservation of SeMet sites is desired. This would not be the case when attempting radiation-induced phasing methods. Higher temperatures will be preferable for RIP phasing if the rate of onset of global nonisomorphism does not increase concomitantly with the specific damage rate. It may also be advisable to use the nano-ice phase of cryoprotectants for RIP phasing attempts, since the specific damage is expected to proceed faster than the overall damage to the crystal.

It cannot be overstated that the presence of heavy atoms in the crystal is to be avoided whenever possible. All the data in this study are normalized to absorbed dose. For a particular sample composition, the ratio of diffraction data gathered to dose will be relatively constant (given a reasonable range of photon energies, dose rate *etc.*) (Murray *et al.*, 2004). However, this ratio will drop considerably if heavy atoms are introduced into the sample. Replacing 1 *M* iodide with fluoride, for example, will make a crystal last more than twice as long.

4.3. Monitoring damage

The degree of damage in a protein crystal could be monitored by a periodic two-point fluorescence measurement of the 'peak' and 'valley' points on the XANES spectrum of the sample (Fig. 1). The ratio of 'peak' to 'valley' counts will reach unity (or less) as the SeMet side chains break down. The crystal would have to be rotated back to the same orientation for these comparisons to avoid confusing damage with XANES anisotropy (Bricogne *et al.*, 2005), and one would have to rapidly switch the endstation back and forth between diffraction mode to fluorescence mode. However, these are not significant technical hurdles at modern X-ray facilities.

In the absence of an 'online' protocol for evaluating XANES during data collection, it is generally advisable to collect a full XANES spectrum after a MAD/SAD data collection has been completed. If the spectrum resembles damaged SeMet, then the data collection from the next crystal should employ a shorter exposure time. Moreover, since the lowest $D_{\frac{1}{2}}$ of SeMet measured is 5 MGy, then a conservative data collection strategy would keep the dose to the sample

below this value. If the SeMet residues in the crystal of interest have larger $D_{\frac{1}{2}}$ values, then a second data set can be collected and merged with the first. It is important to remember that for some 'minimum' exposure time the detector readout noise is still small when compared with the shot noise associated with the background counts on the detector (the square root of the number of background counts). The final data quality from merging many of these 'minimum' exposures will be the same as if the data were collected with longer exposures (with the same total shutter-open time). An advisable strategy is to collect several complete data sets in a row with this 'minimum' exposure time and then merge them together. In this way the point at which radiation damage becomes significant can be determined during data processing.

I would like to thank Brenda Schulman for providing the NE1 protein crystal samples as well as the peptide needed to grow the GCN4 crystals. I would also like to thank Ken Frankel, Scott Classen, Greg Hura and Susan Tsutakawa for helpful discussions on this work and the manuscript. George Meigs and Jane Tanamachi were invaluable for technical support and for organizing blocks of beam time for these demanding experiments, respectively. This work was supported by a University of California Campus-Laboratory Collaboration Grant and grants from the National Institutes of Health: GM74929 and GM24485. Beamline 8.3.1 was funded by the National Science Foundation; the University of California, Berkeley; the University of California, San Francisco and Henry Wheeler. Beamline 12.3.1 and the Advanced Light Source are supported by the Director, Office of Science, Office of Basic Energy Sciences, Materials Sciences Division, of the US Department of Energy under contract No. DE-AC02-05CH11231 at Lawrence Berkeley National Laboratory.

References

Banumathi, S., Zwart, P. H., Ramagopal, U. A., Dauter, M. & Dauter, Z. (2004). *Acta Cryst.* D**60**, 1085–1093.

Box, H. R. (1977). *Radiation Effects: ESR and ENDOR Analysis.* London: Academic Press.

Bricogne, G., Capelli, S. C., Evans, G., Mitschler, A., Pattison, P., Roversi, P. & Schiltz, M. (2005). *J. Appl. Cryst.* **38**, 168–182.

Burmeister, W. P. (2000). *Acta Cryst.* D**56**, 328–341.

Carugo, O. & Carugo, K. D. (2005). *Trends Biochem. Sci.* **30**, 213–219.

Douzou, P. (1977). *Cryobiochemistry.* New York: Academic Press.

Dubnovitsky, A. P., Ravelli, R. B. G., Popov, A. N. & Papageorgiou, A. C. (2005). *Protein Sci.* **14**, 1498–1507.

Durham, P. J., Pendry, J. B. & Hodges, C. H. (1981). *Solid State Commun.* **38**, 159–162.

Fioravanti, E., Vellieux, F. M. D., Amara, P., Madern, D. & Weik, M. (2007). *J. Synchrotron Rad.* **14**, 84–91.

Forziati, A. F., Glasgow, A. R., Willingham, C. B. & Rossini, F. D. (1946). *J. Res. Natl. Bur. Stand.* **36**, 129–136.

Fuhrmann, C. N., Kelch, B. A., Ota, N. & Agard, D. A. (2004). *J. Mol. Biol.* **338**, 999–1013.

Garman, E. & Nave, C. (2002). *J. Synchrotron Rad.* **9**, 327–328.

Garrett, B. C. *et al.* (2005). *Chem. Rev.* **105**, 355–389.

Gonzalez, A., Denny, R. & Nave, C. (1994). *Acta Cryst.* D**50**, 276–282.

Gonzalez, A., von Delft, F., Liddington, R. C. & Bakolitsa, C. (2005). *J. Synchrotron Rad.* **12**, 285–291.

Helliwell, J. R., Ealick, S., Doing, P., Irving, T. & Szebenyi, M. (1993). *Acta Cryst.* D**49**, 120–128.

Higgins, P. D., Attix, F. H., Hubbell, J. H., Seltzer, S. M., Berger, M. J. & Sibata, C. H. (1992). Internal Report 4812. National Institute of Standards and Technology Physics Laboratory, Gaithersburg, MD, USA.

Holton, J. M. (2005). *Annual Meeting of the American Crystallographic Association*, Orlando, FL, USA. Abstract W0308.

Holton, J. M. & Alber, T. (2004). *Proc. Natl. Acad. Sci. USA*, **101**, 1537–1542.

Honig, B. & Nicholls, A. (1995). *Science*, **268**, 1144–1149.

Howard, F. L., Mears, T. W., Fookson, A., Pomerantz, P. & Brooks, D. B. (1947). *J. Res. Natl. Bur. Stand.* **38**, 365–395.

Huang, D. T., Miller, D. W., Mathew, R., Cassell, R., Holton, J. M., Roussel, M. F. & Schulman, B. A. (2004). *Nature Struct. Mol. Biol.* **11**, 927–935.

Hubbell, J. H. (1982). *Int. J. Appl. Radiat. Isotopes*, **33**, 1269–1290.

Kerr, A. (2000). In *CRC Handbook of Chemistry and Physics 1999–2000: A Ready-Reference Book of Chemical and Physical Data (CRC Handbook of Chemistry and Physics)*, 81st ed., edited by D. R. Lide. Boca Raton, FL: CRC Press.

Leiros, H. K. S., McSweeney, S. M. & Smalas, A. O. (2001). *Acta Cryst.* D**57**, 488–497.

Leiros, H. K. S., Timmins, J., Ravelli, R. B. G. & McSweeney, S. M. (2006). *Acta Cryst.* D**62**, 125–132.

MacDowell, A. A. *et al.* (2004). *J. Synchrotron Rad.* **11**, 447–455.

McMaster, W. H., Del Grande, N. K., Mallett, J. H, & Hubbell, J. H. (1969). Report UCRL-50174. Lawrence Livermore National Laboratory, USA.

Milligan, J. R. & Ward, F. (1994). *Radiat. Res.* **137**, 295–299.

Murray, J. W. & Garman, E. F. (2002). *J. Synchrotron Rad.* **9**, 347–354.

Murray, J. W., Garman, E. F. & Ravelli, R. B. G. (2004). *J. Appl. Cryst.* **37**, 513–522.

Murray, J. W., Rudiño-Piñera, E., Owen, R. L., Grininger, M., Ravelli, R. B. G. & Garman, E. F. (2005). *J. Synchrotron Rad.* **12**, 268–275.

Nanao, M. H., Sheldrick, G. M. & Ravelli, R. B. G. (2005). *Acta Cryst.* D**61**, 1227–1237.

Nave, C. & Garman, E. F. (2005). *J. Synchrotron Rad.* **12**, 257–260.

Nave, C. & Hill, M. A. (2005). *J. Synchrotron Rad.* **12**, 299–303.

Newton, A. (1963). *Radiation Effects on Organic Materials*, edited by R. O. Bolt and J. G. Carroll. New York: Academic Press.

Nukaga, M., Mayama, K., Hujer, A. M., Bonomo, R. A. & Knox, J. R. (2003). *J. Mol. Biol.* **328**, 289–301.

Petrik, N. G. & Kimmel, G. A. (2003). *Phys. Rev. Lett.* **90**, 269–270.

Petrik, N. G. & Kimmel, G. A. (2004). *J. Chem. Phys.* **121**, 3736–3744.

Pickering, I. J., Brown, G. E. & Tokunaga, T. K. (1995). *Environ. Sci. Technol.* **29**, 2456–2459.

Pickering, I. J., George, G. N., Van Fleet-Stalder, V., Chasteen, T. G. & Prince, R. C. (1999). *J. Biol. Inorg. Chem.* **4**, 791–794.

Pogocki, D., Ghezzo-Schoneich, E. & Schoneich, C. (2001). *J. Phys. Chem. B*, **105**, 1250–1259.

Rauk, A., Armstrong, D. A. & Fairlie, D. P. (2000). *J. Am. Chem. Soc.* **122**, 9761–9767.

Ravelli, R. B. G., Leiros, H. K. S., Pan, B. C., Caffrey, M. & McSweeney, S. (2003). *Structure*, **11**, 217–224.

Ravelli, R. B. G. & McSweeney, S. M. (2000). *Structure*, **8**, 315–328.

Ravelli, R. B. G., McSweeney, S., Aragao, D. & Caffrey, M. (2000). *Biophys. J.* **78**, 484*a*.

Ravelli, R. B. G., Nanao, M. H., Lovering, A., White, S. & McSweeney, S. (2005). *J. Synchrotron Rad.* **12**, 276–284.

Roberts, B. R., Wood, Z. A., Jonsson, T. J., Poole, L. B. & Karplus, P. A. (2005). *Protein Sci.* **14**, 2414–2420.

Sarret, G., Avoscan, L., Carriere, M., Collins, R., Geoffroy, N., Carrot, F., Coves, J. & Gouget, B. (2005). *Appl. Environ. Microbiol.* **71**, 2331–2337.

Soirat, A. J. A., Wong, C. F., Osman, R. & Weinstein, H. (1997). *J. Comput. Chem.* **18**, 888–901.
Thomazeau, K., Curien, G., Thompson, A., Dumas, R. & Biou, V. (2001). *Acta Cryst.* D**57**, 1337–1340.
Van Fleet-Stalder, V., Chasteen, T. G., Pickering, I. J., George, G. N. & Prince, R. C. (2000). *Appl. Environ. Microbiol.* **66**, 4849.
Weik, M., Berges, J., Raves, M. L., Gros, P., McSweeney, S., Silman, I., Sussman, J. L., Houee-Levin, C. & Ravelli, R. B. G. (2002). *J. Synchrotron Rad.* **9**, 342–346.
Weik, M., Ravelli, R. B. G., Kryger, G., McSweeney, S., Raves, M. L., Harel, M., Gros, P., Silman, I., Kroon, J. & Sussman, J. L. (2000). *Proc. Natl. Acad. Sci. USA*, **97**, 623–628.
Weik, M., Ravelli, R. B. G., Silman, I., Sussman, J. L., Gros, P. & Kroon, J. (2001). *Protein Sci.* **10**, 1953–1961.
Weik, M., Schreurs, A. M. M., Leiros, H. K. S., Zaccai, G., Ravelli, R. B. G. & Gros, P. (2005). *J. Synchrotron Rad.* **12**, 310–317.
Woolfson, M. M. (1970). *An Introduction to X-ray Crystallography*, 2nd ed. Cambridge University Press.
Yano, J., Kern, J., Irrgang, K. D., Latimer, M. J., Bergmann, U., Glatzel, P., Pushkar, Y., Biesiadka, J., Loll, B., Sauer, K., Messinger, J., Zouni, A. & Yachandra, V. K. (2005). *Proc. Natl. Acad. Sci. USA*, **102**, 12047–12052.
Zwart, P. H., Banumathi, S., Dauter, M. & Dauter, Z. (2004). *Acta Cryst.* D**60**, 1958–1963.